Ball-milled magnetite for efficient arsenic decontamination: Insights into oxidation–adsorption mechanism

Published in: *Journal of Hazardous Materials*

Citation for published version: Yang, X., Liu, S., Liang, T., Yan, X., Zhang, Y., Zhou, Y., Sarkar, B., Ok, Y.S., (2022) Ball-milled magnetite for efficient arsenic decontamination: Insights into oxidation–adsorption mechanism. *Journal of Hazardous Materials*. 427: 128117. doi: 10.1016/j.jhazmat.2021.128117.

Document version: Accepted peer-reviewed version.

Ball-milled magnetite for efficient arsenic decontamination: Insights into oxidation–adsorption mechanism

Xiao Yang[a], Siyan Liu[a,b], Tao Liang[a,b], Xiulan Yan[a,*], Yunhui Zhang[c], Yaoyu Zhou[d], Binoy Sarkar[e], Yong Sik Ok[f,]**

[a] Key Laboratory of Land Surface Pattern and Simulation, Institute of Geographic Sciences and Natural Resources Research, Chinese Academy of Sciences, Beijing 100101, China

[b] College of Resources and Environment, University of Chinese Academy of Sciences, Beijing 100190, China

[c] College of Environmental Science and Engineering, Tongji University, Shanghai, 200092, China

[d] College of Resources and Environment, Hunan Agricultural University, Changsha, 410128, China

[e] Lancaster Environment Centre, Lancaster University, Lancaster, LA1 4YQ, United Kingdom

[f] Korea Biochar Research Center, O-Jeong Eco-Resilience Institute (OJERI) & Division of Environmental Science and Ecological Engineering, Korea University, Seoul 02841, Republic of Korea

---

* Corresponding author: yanxl@igsnrr.ac.cn (X. Yan); yongsikok@korea.ac.kr (Y.S. Ok).

Highlights:

- Ball-milled modified magnetite exhibited high stability and As-adsorption capacity.
- Dry ball milling facilitated the formation of hydroxyl and carboxyl groups upon the magnetite.
- Roles of surface functional groups and reactive oxygen species during the As adsorption were discussed.
- Enhanced As(III) removal was achieved via oxidation-adsorption mechanism.

Graphical Abstract:

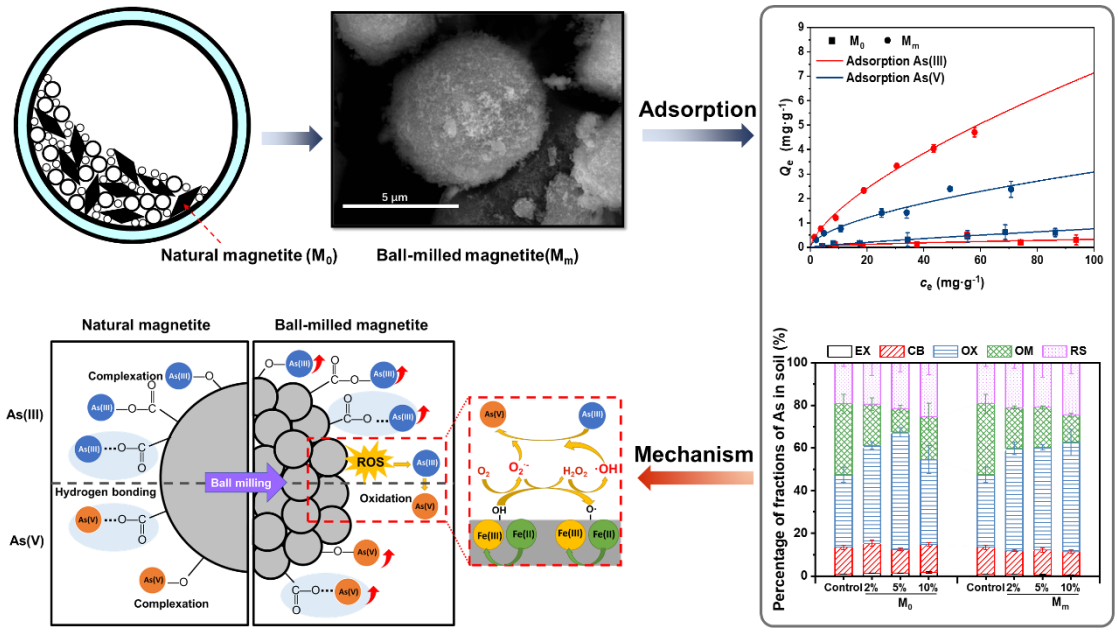

Abstract

Conventional adsorbents for decontaminating arsenic exhibit low efficacy for the removal of arsenite (As(III)). This study aims to develop a robust As adsorbent from natural magnetite (M_0) via a facile ball milling process, and evaluate their performance for decontaminating As(III) and As(V) in water and soil systems. The ball milling process decreased the particle size and crystallinity of M_0, resulting in pronounced As removal by the ball-milled magnetite (M_m). Ball milling under air facilitated the formation of Fe-OH and Fe-COOH functional groups on M_m interface, contributing to effective elimination of As(III) and As(V) via hydrogen bonding and complexation mechanisms. Synergistic oxidation effects of hydroxyl and carboxyl groups, and reactive oxygen species ($O_2^{\cdot-}$, and ·OH) on the transformation of As(III) to As(V) during the adsorption were proposed to explain the enhanced As(III) removal by M_m. A short-term soil incubation experiment indicated that the addition of M_m (10 wt%) induced a decrease in the concentration of exchangeable As by 30.25%, and facilitated the transformation of water-soluble As into residual fraction. Ball milling thus is considered as an eco-friendly (chemical-free) and inexpensive (scalable, one-stage process) method for upgrading the performance of natural magnetite towards remediating As, particularly for tackling the highly mobile As(III).

Keywords: Arsenic, Magnetite, Ball milling, Synergistic oxidation, Sustainable environmental engineering.

1. Introduction

Arsenic (As) is an omnipresent contaminant in soil, water, and atmosphere. The undesirable emission of As-bearing substances results in extensive ecological problems owing to the high migration ability and ecotoxicity of these substances (Turunen et al., 2016). These toxins can enter the food chain primarily via crops cultivated on contaminated soil and/or irrigation water, and intake of polluted drinking water (Chen et al., 2020), thereby posing significant health risk to plants, animals, and humans (Zhang et al., 2017). Approximately 140 million people across 50 countries are exposed to water with As contents significantly higher than the provisional guideline of 10 $\mu g \cdot L^{-1}$ established by the World Health Organization (WHO, 1993). The predominant As species in groundwater and soil are comprised of As(III) and As(V). The apparent toxicity and mobility of As(III) are higher than those of As(V). The coexistence and transformation of As(III) and As(V) should also be considered within the pH range of 6-9 in natural aquifers (Shankar et al., 2014). Therefore, development of efficient As(III)/As(V) decontamination protocols for both water and soil is a global research need.

Several methods have been intensively implemented for the removal of As from soil and water. Primary efforts for reducing human exposure to As involve the development of affordable and sustainable techniques for the simultaneous removal of As(III) and As(V), while avoiding any secondary adverse effects on the local environments (Khalid et al., 2017). Chemical precipitation/flocculation, ion exchange, reverse osmosis, nanofiltration, and adsorption are the commonly used methods to remove As from drinking water (Bhardwaj et al., 2019). Meanwhile, adsorption is considered feasible approach for eliminating As(III) from water due to high efficiency, cost-effectiveness, and ease of operation. To mitigate soil arsenic

pollution, solidification/stabilization, backfilling, phytoremediation, and electric remediation are applied (Miretzky and Cirelli, 2010). Potent adsorbents can also be used to mitigate soil As contamination via stabilization, thereby lowering the bioavailability and migration of As species in the soil (Yang et al., 2021). However, it is challenging to design and synthesize adsorbent/stabilizer materials with a high affinity for both As(III) and As(V).

Recently, applying Fe-containing minerals, such as magnetite (Fe_3O_4), maghemite (γ-Fe_2O_3), hematite (α-Fe_2O_3), goethite (α-FeOOH), ferrihydrite ($Fe_{10}O_{14}(OH)_2$), lepidocrocite (FeO(OH)), and siderite ($FeCO_3$), has received a momentum for As removal from water (Liu et al., 2014). Among them, the synthesized magnetite nanoparticles (MNPs) have high As affinity and are magnetically separable. Wojciechowska and Lendzion-Bieluń (2020) confirmed that MNPs prepared by co-precipitation method has a small size and a large specific surface area, and the dose of 2.5 $g \cdot L^{-1}$ achieved the adsorption degree of 97-99% (initial concentration of As(V): 10 $mg \cdot L^{-1}$ at pH=7). Partial substitution of MNPs with natural magnetite can avoid the indispensable harmful chemicals used in the synthesis, create mutual benefit in green-adsorbent development and market requirement. Nonetheless, natural magnetite shows a heterogeneity in its properties and low adsorption efficiency for As, thereby limiting its engineering applications (Su, 2017). Therefore, modifying the natural magnetite into powerful As(III)/As(V) adsorbent has become an urgent need.

Common modification methods of magnetite include: 1) incorporation with other components to form a composite material with high specific surface area and adsorption capacity for As(III)/As(V); 2) functionalization with surfactants comprising hydroxyl, amino, or carboxylic acid groups and polymer chitosan to form coatings on magnetite, thereby

increasing the presence of surface functional groups; and 3) use of oxidants to oxidize As(III) to As(V) and then remove As(V) (Medina et al., 2019; Zhong et al., 2021). Compared with chemical modification methods, ball milling is a solid-to-solid means with no need of harmful chemicals (Wang et al., 2021b). It not only can rapidly reduce the particle size (Nandiyanto et al., 2018), but introduce structure changes that generate defects and fresh fracture surfaces (Petrovský et al., 2000), as well as alter surface chemistry of materials that increase the oxygen-containing functional groups into a mineral interface. For example, Matović et al. (2019) compared the variation in the number of oxygen-containing functional groups introduced in activated carbon cloth via ball milling under air and argon atmospheres. Both conditions increased the total number of functional groups; the concentration of functional groups on the surface was higher under air (4.0907 $mmol \cdot g^{-1}$) than under argon (3.8346 $mmol \cdot g^{-1}$). Such changes allow for an active adsorption surface, and attain the goal of efficient As removal.

The results obtained in previous studies validated the potential of oxidation–adsorption mechanisms for effective As(III) decontamination (Ma et al., 2020). We hypothesized that magnetite may exhibit excellent oxidizing ability via manipulating the Fe-related functional groups on the surface matrix to promote As(III) oxidation. This will result in pronounced As decontamination. The synergistic role of oxygen-containing functional groups and reactive oxygen species (ROS), with the use of ball-milled magnetite, during the treatment of As-contaminated water was comprehensively discussed. We characterized the physical and chemical properties of natural and ball-milled magnetite, and evaluated the adsorption capacities of these adsorbents for As(III) and As(V). Furthermore, the governing mechanisms of As adsorption by magnetite before and after ball milling were elucidated. Finally, the use of

magnetite to stabilize As-polluted soil was investigated with respect to the application rate.

2. Materials and methods

2.1 Chemicals and reagents

Natural magnetite (M_0) was collected from an iron ore mine in Hebei Province, China, located at 40°00′39″N, 118°51′22″E. M_0 was washed with deionized water, pulverized by the coarse jaw crusher (LHMY-60, Shuangjin Machinery Company, China) and passed through a 200-mesh mm sieve. The chemical compositions of M_0 are shown in Table S1. All the chemicals used were of guaranteed reagent (GR) grade, and they were purchased from Sinopharm Chemical Reagent Co. Ltd., Shanghai, China. Deionized (DI) water (Direct-Q3, MilliporeSigma, Massachusetts, USA) was used in all the experiments.

2.2 Preparation of magnetite via ball milling

Planetary ball milling (MITR-YXQM-2L, Miqi Instrument Equipment Co. Ltd., Changsha, China) was performed under ambient conditions. The samples were ball-milled using an agate tank in association with agate balls under solvent-free conditions. The ball-to-magnetite mass ratio was 10:1. The rotation frequency was maintained at 640 rpm for 12 h. The as-modified product was denoted as M_m, and stored in a desiccator before use.

2.3 Characterization of magnetite

Characterizations of chemical composition (elemental analyzer), morphology (scanning electron microscopy combined with energy-dispersive X-ray spectroscopy (SEM-EDS)), structural properties (X-ray diffraction (XRD) and Raman spectroscopy), crystallinity and porosity (N_2 adsorption-desorption isotherm analysis), surface chemistry (X-ray photoelectron

spectroscopy (XPS) and Fourier-transform infrared (FTIR)), Zeta potentials, magnetism (vibrating sample magnetometry (VSM)), ROS species (electron paramagnetic resonance (EPR)), and electrochemical properties (electrochemical impedance spectra (EIS)) are presented in detail in Text S1 of the Supplementary Material.

2.4 Adsorption experiments

Batch experiments were performed to evaluate the As-adsorption capacities of M_0 and M_m, and the specific experimental procedure was described in Text S2. The meanings and equations of different kinetic (pseudo-first-order, pseudo-second-order, Elovich, and Weber–Morris models) and isotherm (Langmuir, Freundlich, Temkin, and Dubinin–Radushkevich) models were summarized in Table S2, Table S3.

To elucidate the variations in As(III)- and As(V)-adsorption capacities of M_0 and M_m, the site energy distribution of the adsorbents was deduced from the isotherm parameters and expressed as follows:

$$Q_e(C_e) = \int_0^{+\infty} Q_h(E, C_e)\, F(E) dE \quad (1)$$

where $Q_e(C_e)$ is the total adsorption of solute on the adsorbent, $Q_h(E,C_e)$ represents the isotherm over local adsorption sites with an adsorption energy of E (kJ·mol^{-1}), and $F(E)$ is the site energy frequency distribution over a range of sites with homogeneous energies. The adsorption energy, E, indicates the difference between the adsorption energies of the solute and solvent at a specific adsorption site. The range is usually considered as (0,+∞) owing to the unknown adsorption site energies.

The relation between C_e of the adsorbent and E, based on the condensation approximation,

is expressed as follows:

$$C_e = C_s \exp\left(-\frac{E - E_s}{RT}\right) = C_s \exp(-\frac{E^*}{RT}) \quad (2)$$

where C_s is the solute solubility in the solvent (mg·L^{-1}), E_s is the lowest physically realizable sorption energy (kJ·mol^{-1}), and E* is the lowest bond energy for adsorption at the equilibrium concentration of C_e (kJ·mol^{-1}).

The adsorption isotherm model can be described as a function of $Q_e(E^*)$ related to E*, based on the relationship between C_e and E*. The site energy distribution function, $F(E^*)$, (mg·mol) (kg·J)$^{-1}$ can be obtained by deriving $Q_e(E^*)$:

$$F(E^*) = -\frac{\mathrm{d}Q_e(E^*)}{\mathrm{d}E^*} \quad (3)$$

The mathematical expectation (μ) and standard deviation (σ) of E*, based on the site energy distribution, were calculated to determine the average site energy (E_m, kJ·mol^{-1}) and the heterogeneous adsorption sites of the two magnetite materials for As(III) and As(V) (Zhang et al., 2021).

$$E_m = \mu(E^*) \quad (4)$$

$$\sigma = \sqrt{\mu(E^{*2}) - \mu(E^*)^2} = \sqrt{\mu(E^{*2}) - {E_m}^2} \quad (5)$$

2.4 Soil chemical analysis and stabilization

Surface soil samples (0–20 cm) were collected from a contaminated agricultural soil in Qinglong County, Hebei Province, China (40°22′36″N, 118°43′14″E). The soil samples were air-dried, mildly crushed, and sieved through a 10-mesh sieve (<2 mm). The main physicochemical properties of the soil samples are listed in Table 1.

Table 1

A series of short duration batch experiments was performed to quickly examine the effects of magnetite addition on As stabilization in soil. A varied dosage of M_0 and M_m, with a magnetite-to-soil mass ratio of 2, 5, and 10%, was added to 100 g of the soil. The liquid-solid ratio was adjusted to 1:4 using DI water, and the samples without adding magnetite were considered as the control group. The mixed samples were incubated at 25 °C using an artificial climate box for 7 days. The five-step sequential extraction procedure was conducted followed by Wenzel et al. (2001): (1) exchangeable (EX); (2) bound to carbonates (CB); (3) bound to Fe-Mn oxides (OX); (4) bound to organic matter (OM); and (5) residual (RS), for the incubated soils. The concentrations of total As and five fractions of As were analyzed using AFS coupled with liquid chromatography (LC-AFS; AFS 9130, Titan Instruments Co. Ltd., Beijing, China). The soil pH was determined using the 2.5:1 soil/H_2O method (Yan et al., 2020b). Each treatment was repeated thrice.

2.5 Statistical analysis

Statistical analysis was performed via one-way analysis of variance, and the least significant difference (LSD) test was used to compare the mean values using IBM SPSS Statistics 19.0 for Windows. The data were presented as the mean ± standard error.

3. Results and discussion

3.1 Characterization of natural and ball-milled magnetite

3.1.1 Structural information and surface morphology

The XRD results confirmed the presence of magnetite (Fe_3O_4), maghemite (γ-Fe_2O_3), hematite (α-Fe_2O_3) and siderite ($FeCO_3$) phases in M_0 and M_m (ICSD card number: 01-076-

200 1849, 01-039-1346, 01-085-0599 and 01-083-1764). Ball milling changed the full width half
201 maximum of the high-intensity reflection at $2\theta = 35.441°$ of M_0 and M_m from 0.193° to 0.755°.
202 The crystallite sizes for M_0 (43.1 nm) sharply decreased compared to that of M_m (11.0 nm). The
203 decrease in crystalline size might induce an increase in stacking faults and structural disordering.
204 This resulted in substantial peak broadening, indicating periodic damage to the crystal lattice
205 occurred (Tung et al., 2009). Natural magnetite was crystalline; however, the height and width
206 of the diffraction peaks decreased and increased, respectively, after ball milling, hinting partial
207 decay of the crystallinity. M_m exhibited more amorphous, higher disorder and number of surface
208 defects than M_0, allowing for M_m may have more active sites for adsorbing As (Yuan et al.,
209 2019). Furthermore, the characteristic peak of siderite disappeared after ball milling because
210 siderite might be decomposed with the participation of oxygen ($FeCO_3 + 1/2\ O_2 \rightarrow Fe_3O_4 +$
211 CO_2) (Mora–Mendoza et al., 2019).

212 Raman spectroscopy was performed to analyze the chemical bonding and intramolecular
213 bonds (Fig. 1b). Five Raman-active bands was identified via factor group analysis of M_0 and
214 M_m: A_{1g}, E_g, and three T_{2g} (Moon et al., 2010). Both M_0 and M_m presented a magnetite A_{1g} mode
215 at 655 cm^{-1} that was assigned to a symmetric stretch of oxygen atoms in conjunction with Fe–
216 O bonds (Wang et al., 2009). For M_m, the T_{2g} mode band at 283 cm^{-1} broadened and redshifted
217 to the hematite E_g mode (290 cm^{-1}). This behavior is likely due to stress effects on the surface
218 of the nanocrystals (Mendili et al., 2016). The weak peak around 205 cm^{-1} as the T_{2g} model
219 originated from vibrations of Fe^{3+} and O^{2-} (Shebanova et al., 2003), which disappeared after
220 the ball milling. M_0 presented characteristic absorption peaks at 388 cm^{-1} corresponding to
221 maghemite T_{2g}, which was consistent with the observations in XRD patterns (Peng et al., 2015).

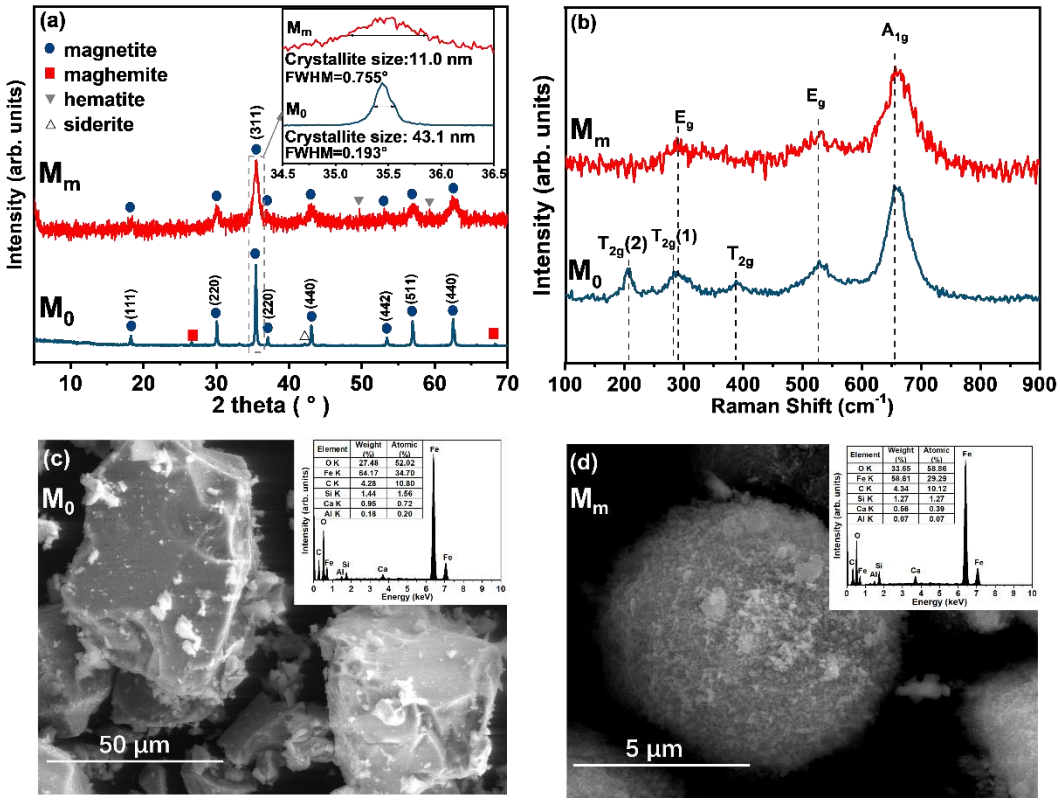

222 **Fig. 1** Structural characterization and morphological features of the magnetite sample before
223 and after ball milling. (a) XRD patterns; (b) Raman spectra; (c, d) SEM images (inset: EDS
224 mapping). M_0 and M_m denote natural magnetite and ball-milled magnetite, respectively.

225

226 The SEM images of M_0 illustrated the presence of irregular, micron-scale, nonporous, and
227 loosely packed particles that were transformed into submicron spherical particles after ball
228 milling. Initially, the particles were broken into polygonal particles primarily during the milling
229 and then the particle shapes became blunt and smooth with the action of friction and shear (Lai
230 and Chen, 2017). The free surface energy increased owing to fracture of the powder, thereby
231 increasing the presence of atomic dislocations (Byrne et al., 2016). Ball milling dramatically
232 increased the specific surface area, by 34.48-fold, and total pore volume, by 33.00-fold, than
233 those of the natural magnetite; however, the average pore diameter remained approximately

234 unchanged (Table 2). The EDS mapping and elemental analyzer indicated that both surface and
235 bulk O and H contents were multiplied after ball milling, and approximately 1.4 wt% of C was
236 detected in two samples that could come from the siderite or the organic impurities (Mora–
237 Mendoza et al., 2019; Wang et al, 2020). These observations agree well with the previous
238 literatures, which probably due to the oxygen and moisture inside the reactor was introduced
239 onto the newly generated interface of magnetite during ball milling, forming a highly reactive
240 surface (Table 2) (Kumar et al., 2020; Xu et al., 2021).

241 **Table 2**

242 **3.1.2 Analysis of surface chemistry and magnetic properties**

243 Fig. 2a shows the FTIR spectra of various functional groups in M_0 and M_m. The peaks at
244 3421 and 1094 cm^{-1} can be ascribed to O–H stretching vibration and the absorption band of
245 hydroxyl group, and the O–Si–O combination bands (1639 cm^{-1}) and the Fe–OH stretching
246 groups (1016 cm^{-1}) are also presented. The Fe–O stretching groups, where bands at 570 and
247 458 cm^{-1} represent the positions of the octahedron and tetrahedron, respectively (Salem et al.,
248 2013). The Fe–O bond provided an extended lattice framework, which would potentially
249 increase the number of octahedral holes to capture more As cations (Ellis et al., 1993).
250 Specifically, M_m has a new COO– stretching vibration group (1489 cm^{-1}) compared to M_0,
251 which may due to the siderite decomposition or the cracking of organic impurities in
252 mechanochemical processes (Liu et al., 2015a).

253 Fig. 2b–c and Fig. S1a-b present the high-resolution deconvoluted XPS spectra for M_0 and
254 M_m. The binding energy peaks at ~709 and 711 eV correspond to Fe(II) and Fe(III) in octahedral
255 coordination, and at 714 eV is attributed to Fe(III) in tetrahedral coordination of Fe_3O_4

256 (Srivastava et al., 2018). The peak at ~724 and 719 eV are associated with Fe $(II)_{sat}$ and Fe
257 $(III)_{sat}$. Results indicated that charge transfer between Fe(II) and Fe(III) was followed by the
258 existence of a mixed oxide in magnetite. The atomic ratios of Fe(III) to Fe(II) ions shifted from
259 1.76 for M_0 to 2.11 for M_m, respectively, suggesting that the surface of M_0 was oxidized during
260 ball milling in the atmosphere of air. The peak of O 1s at ~529.8 eV (Fig. 2b) revealed that the
261 introduced O atoms reacted with surface Fe to form Fe-bound oxygen species (FeO_x, Fe_3O_4,
262 and FeOOH) (Zhang et al., 2019). The peak at 530.6 eV resulted from the lattice oxygen in
263 Fe_3O_4 (Han et al., 2017) and the content of lattice oxygen increased from 29.19% to 35.59%
264 due to ball milling. The increase of lattice oxygen may aid to form an environment with high O
265 activity and accelerate the oxidation reaction. This because the improved electron transfer of
266 oxygen-containing functional groups (Zheng et al., 2019).

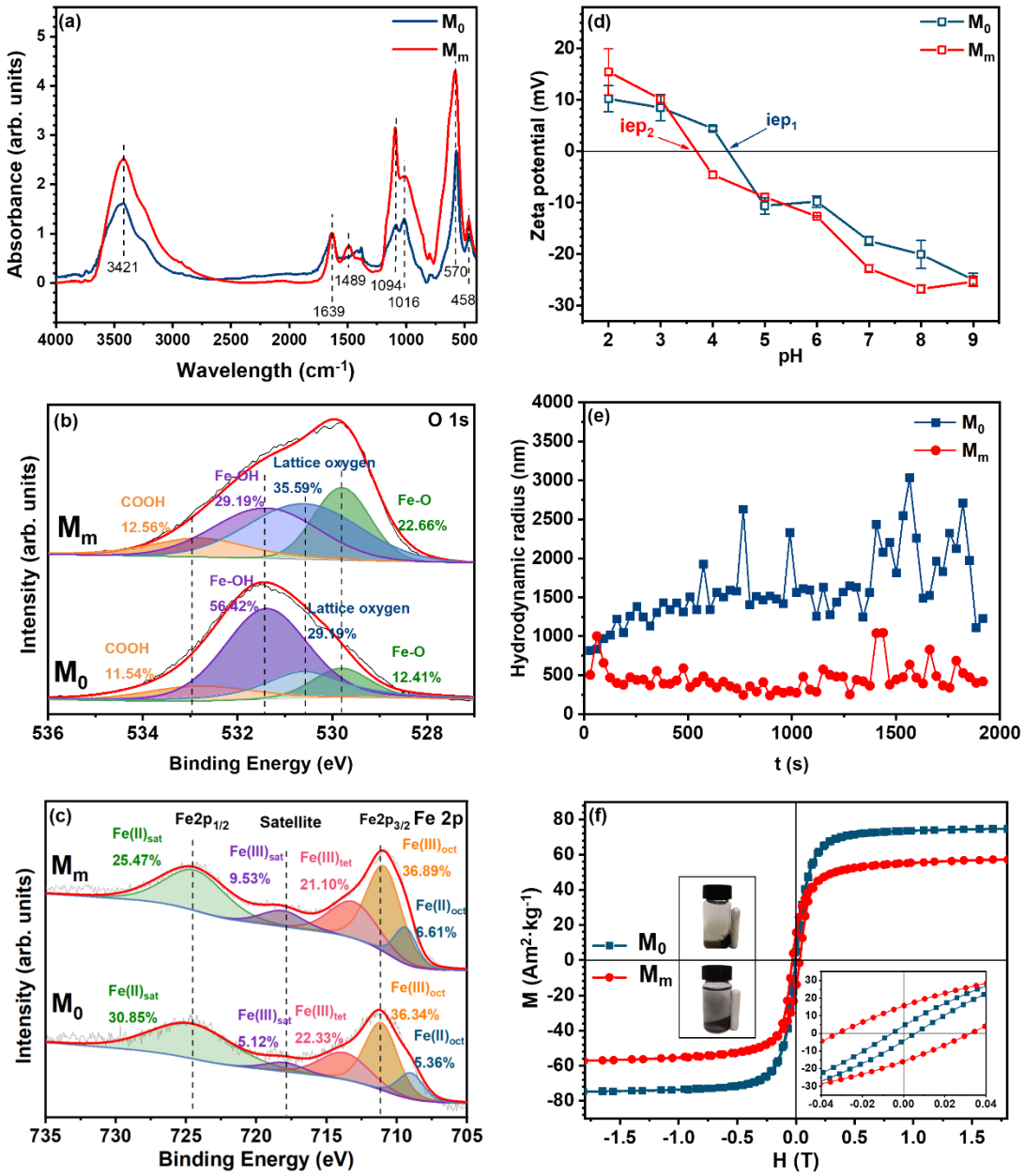

267

268 **Fig. 2** Analytical measurements of the magnetite sample before and after ball milling. (a) FTIR

269 spectra; (b, c) O 1s, Fe 2p signals recorded via XPS; (d) zeta potential changes as function of

270 pH; (e) hydrodynamic radius; and (f) magnetic properties recorded via VSM (inset: the

271 photographs of magnetite particles were placed in a magnetic field). M_0 and M_m denote natural

272 magnetite and ball-milled magnetite, respectively.

The overall trends of the zeta potentials of M_0 and M_m varied consistently with an increase in pH (Fig. 2d). High zeta potentials (either negative or positive) indicate the presence of electrically stable particles (Samimi et al., 2019), revealing that the magnetite is more stable at neutral pH after ball milling. The sign of the zeta potential for M_0 was reversed at pH 4.3. This was recognized as the isoelectric point (*iep*), and the *iep* of M_m decreased to pH 3.6. The M_m had a smaller hydrodynamic radius than the natural at 298 K (Fig. 2e). Ball milling can improve the stability and aggregation of particles in the aqueous solution. Nevertheless, the rising in hydroxyl and carboxyl groups made the magnetite's surface characteristics more hydrophilic, which is propitious to the arsenic removal (Veloso et al., 2020).

The magnetic hysteresis curves of M_0 and M_m are presented in Fig. 2f. Both the adsorbents were ferromagnetic in nature owing to the low coercivity (H_{ci}) and remanence (M_r) values (Ahmadzadeh et al., 2017). Despite ball milling resulted in a slight decrease in the saturation magnetization from 74.69 $Am^2 \cdot kg^{-1}$ (M_0) to 57.44 $Am^2 \cdot kg^{-1}$ (M_m). The insets in Fig. 2f demonstrated the photographs of M_0 and M_m particles placed in a magnetic field for 30 s, representing that magnetic separation of the particles from water was still valid for M_m.

3.2 Adsorptive performance of ball-milled magnetite for As removal from water

3.2.1 Adsorption kinetics

Fig. 3a–b presented the variation in the As(III) and As(V) adsorption capacities with time, and equilibrium was attained after 20 h. The fitting results in Table S4 revealed that the adsorption of As(III) and As(V) by M_0 was consistent with the Weber–Morris model (R^2 = 0.9699 and 0.9562, respectively). The multilinearity of intraparticle diffusion plot of M_0 for

As(III) and As(V) adsorption is shown in Fig. S2, corresponding to two slopes of two primary mechanisms: (I) external mass transfer, and (II) intraparticle diffusion (Largitte et al., 2016). It was inferred that As adsorption on M_0 was a two-step process involving initial mass transfer of the adsorbate molecule to the magnetite boundary layer and subsequent adsorbate diffusion into magnetite. Internal diffusion depends on the extent of surface reaction and pore structure of the adsorbent, resulting in a slow reaction rate (Pholosi et al., 2020). Differently, the kinetic data of M_m exhibited an optimal fit, under neutral conditions, to the pseudo-second-order model (R^2 for As(III) and As(V) was 0.9728 and 0.9923, respectively). The theoretical $Q_{e,cal}$ (2.06 and 1.07 $mg \cdot g^{-1}$) was consistent with the experimental $Q_{e,exp}$ (2.11 and 1.03 $mg \cdot g^{-1}$). Ball milling increased the specific surface area and number of adsorption sites of magnetite, forming a heterogeneous surface; furthermore, the process followed the mechanism of binuclear surface adsorption (Dutta et al., 2020), which explained the increased the adsorption capacity and adsorption rate of As by M_m. The adsorption process for M_m was dominated by surface reactions; therefore, it was subsequently controlled by further complexation interactions (Xie et al., 2014).

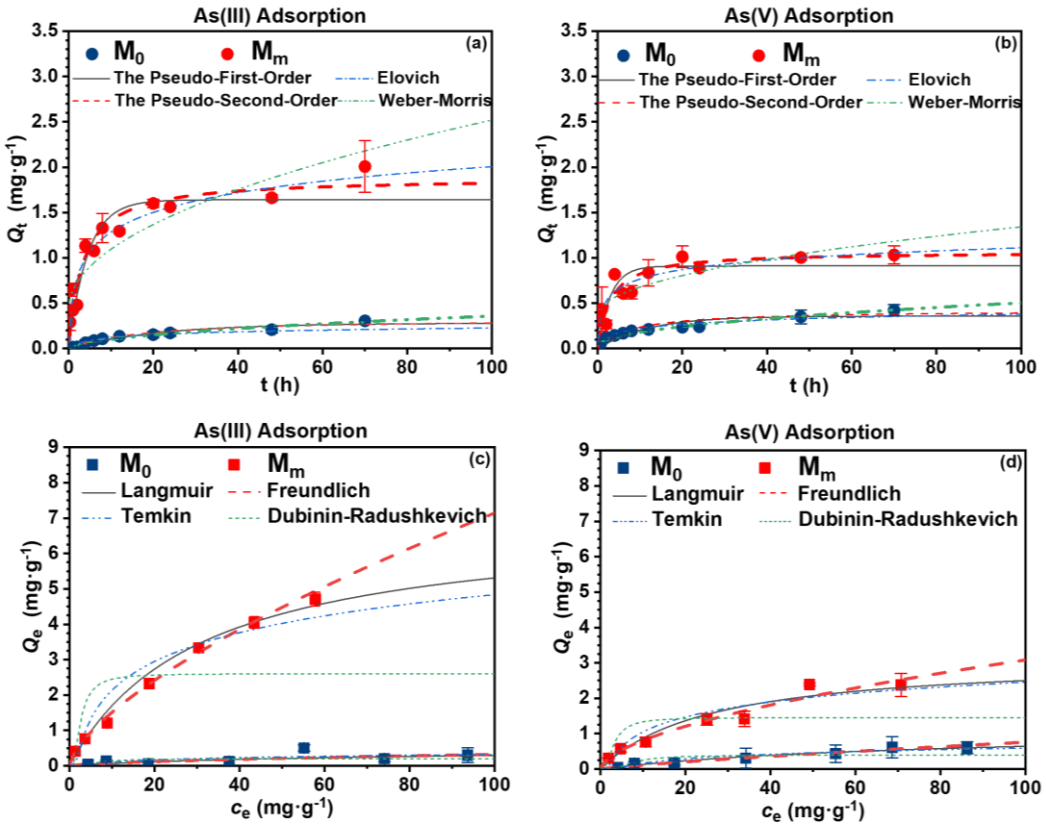

309 **Fig. 3** Adsorption kinetics (a, b) and isotherms (c, d) of the adsorbents. M_0 and M_m denote

310 natural magnetite and ball-milled magnetite, respectively.

311

312 **3.2.2 Adsorption isotherms**

313 Fig. 3c–d displayed the curves describing the concentration, C_e (mg·L^{-1}), vs. adsorption

314 capacity, Q_e (mg·g^{-1}), of As(III) and As(V). Multilayer adsorption occurred in both the materials

315 because the correlation coefficient of the Freundlich model exhibited the optimal fit (Table S5)

316 (Vikrant et al., 2018). The adsorption isotherms of both M_0 and M_m were nonuniform and

317 involved different adsorption forces (Singh et al., 2012). K_F is the adsorption capacity per unit

318 pressure, and a high K_F indicates a strong adsorption capacity. The K_F of M_m for both As(III)

319 and As(V) clearly outweigh the values for M_0. The $1/n$ value is generally less than 1, and its

320 magnitude reflects the influence of adsorbate concentration on the adsorption capacity. The

values of n calculated from the Freundlich model fitting were all greater than 1, thereby indicating their validity for the active adsorption sites (Vikrant et al., 2018). It was inferred that adsorption was an endothermic process and induced disorder at the solid–liquid interface. Moreover, adsorption and oxidation occurred simultaneously between the As species and the adsorbents (Liu et al., 2011).

3.2.3 Site energy distribution

The relationship between the adsorption efficiency for As(III)/As(V) and the site energy distribution on M_0 and M_m was derived using the Langmuir–Freundlich model (Fig. 4a–b). The high-adsorption-energy sites were preferentially occupied because the concentration of As(III)/As(V) was low. As(III) and As(V), with an increase in their concentration, gradually occupied the low-energy sites owing to saturation of a substantial portion of the high-energy sites. The energy of the sites were the dominant contributors to the adsorption of As(III) and As(V) on magnetite shifted from the high- to low-energy side after ball milling. The area occupied by M_m was greater than that occupied by M_0, indicating the pronounced adsorption of As(III)/As(V) on M_m. The high E_m after ball milling signified the strong adsorption affinities of M_m for As(III) (28.98 $kJ \cdot mol^{-1}$) and As(V) (28.44 $kJ \cdot mol^{-1}$). The high σ value indicated the presence of numerous heterogeneous sorption sites. The maximum increase in the number of heterogeneous adsorption sites for As(III) was observed in M_m. The presence of heterogeneous surfaces originated from the heterogeneity in the chemical composition (Shen et al., 2015).

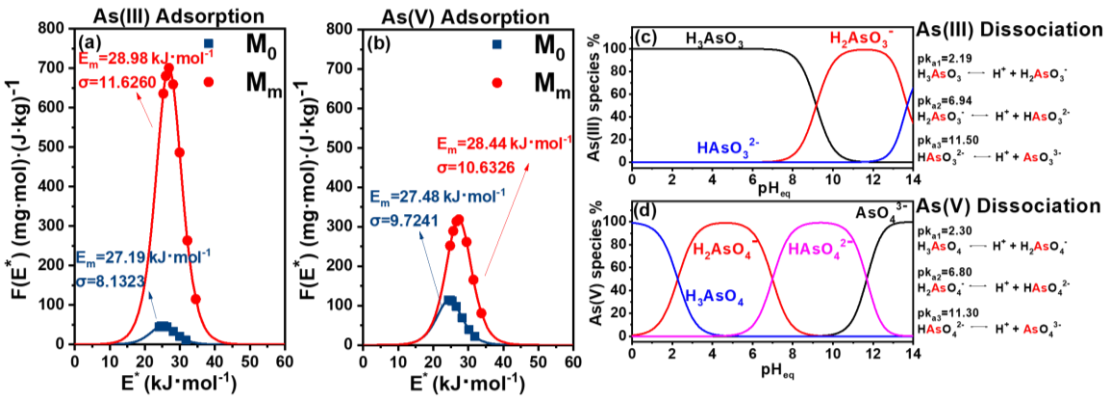

Fig. 4 Site energy distributions for M_0 and M_m after As(III) and As(V) removal (a, b), and variation in As speciation at different pH (c, d). M_0 and M_m denote natural magnetite and ball-milled magnetite, respectively.

3.2.4 Roles of surface functional groups and ROS in As oxidation and adsorption

3.2.4.1 Role of surface functional groups

Fig. 5a–b showed the As 3d spectra obtained via XPS analysis. These results revealed the successful adsorption of As on M_0 and M_m. Arsenic exists in different forms under neutral pH conditions owing to the difference in dissociation constant (pK_a). As(III) and As(V) exist in the form of H_3AsO_3, $H_2AsO_4^-$, and $HAsO_4^{2-}$ (Fig. 4c–d). These anions can interact with hydrogen bond acceptors. The oxygen in Fe-COOH groups functions as H-bond-accepting sites that contribute to capture As (Wu et al., 2020). The O 1s spectra illustrated an increase of carboxyl groups for M_m after the adsorption of As(III) and As(V), affirming that hydrogen bonding could be partly responsible for the As adsorption upon the magnetite adsorbents.

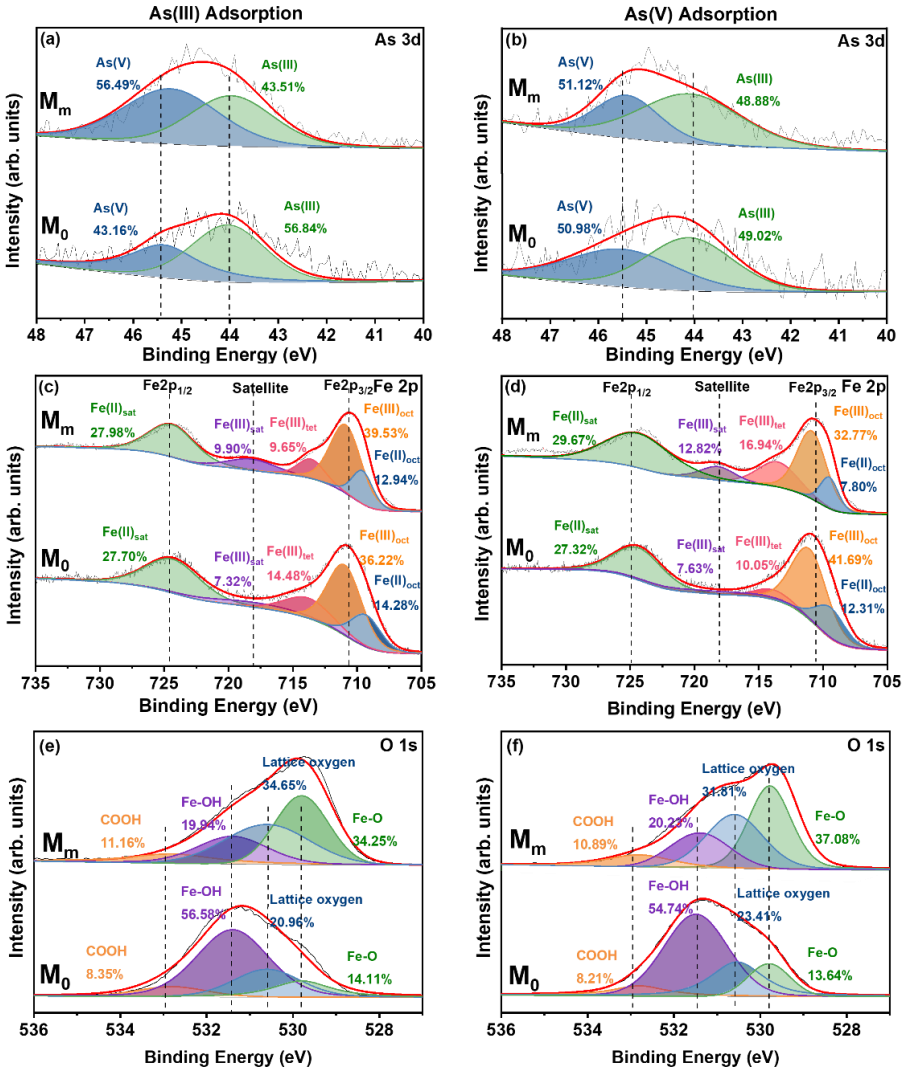

354 **Fig. 5** As 3d (a, b), Fe 2p (c, d), and O 1s (e, f) spectra, obtained via XPS, of adsorbents before
355 and after adsorptive removal of As(III) and As(V). M_0 and M_m denote natural magnetite and
356 ball-milled magnetite, respectively.

357

358 A new low-intensity band, designated as the characteristic peak of Fe–O–As, appeared in
359 the FTIR spectrum at 870 cm^{-1} (Fig. S3a–b). Replacement of Fe-OH on the mineral surface
360 with As to form a surface complex should be one of the main mechanism for both As(V) and
361 As(III) elimination (Perez et al., 2019). Silva et al. (2009) proposed that -COOH groups affected

the mobility of As(V) in an environment under Fe bridging. This would facilitate the hydrogen bonding formation and efficient As adsorption. Besides, the ionizable impurity carbon-based functional groups may acquire charge through protonation and deprotonation with solutes, and result in electrostatic attractions with negatively charged arsenate species (Vithanage et al., 2017). Nevertheless, surface ion-exchange reactions might also play a part during the adsorption process, which illustrated by the following equations (Hao et al., 2018; Peng et al., 2021).

$$\equiv Fe–OH + H_2AsO_4^- \rightarrow \equiv Fe–HAsO_4^- + H_2O \quad (6)$$

$$\equiv Fe–OH + HAsO_4^{2-} \rightarrow \equiv Fe–AsO_4^{2-} + H_2O \quad (7)$$

$$\equiv Fe–OH + H_3AsO_3 \rightarrow \equiv Fe–O–As(OH)_2 + H_2O \quad (8)$$

$$\equiv Fe–COOH + H_3AsO_3 \rightarrow \equiv Fe–COO–As(OH)_2 + H_2O \quad (9)$$

3.2.4.2 Role of ROS

Comparing the As 3d spectra of As (III) adsorbed by magnetite, an increase in As(V) occurred from 43.16% to 56.49% was observed after ball milling; however, an opposite trend was observed for As(III). This suggested the occurrence of a redox reaction between As(V) and As(III) on the surface of the adsorbents. The intensity of the $Fe(II)_{oct}$ peak decreased after As(III) adsorption. The relative contents of $Fe(III)_{oct}$ in M_0 and M_m were 36.22% and 39.53%, respectively. These validated that the occurrence of parallel oxidation of As(III) and Fe(II). Fe atoms in magnetite existed as Fe(II) and Fe(III) mixed-valence states; therefore, cation vacancies were generated at the octahedral sites during the oxidation of Fe(II) octatoms to Fe(III) (Liu et al., 2015b). Either electron migration or Fe(II) diffusion from the internal to the oxidized surface of magnetite might happen, considering the balance of electroneutrality. Zheng et al.

(2021) also proposed that the release of Fe(II) from the mineral surface could take place during adsorbing/oxidizing As(III). Hence, role of reactive Fe(II) is of significance during the redox transformation of adsorbed As (Schaefer et al., 2011).

In addition to the oxidation of adsorbed As(III) via the direct reaction with surface Fe-OH and Fe-COOH groups, some studies claimed that highly oxidizing substances could also impact the oxidation of adsorbed As(III) (Zhong et al., 2018). We propose that the As(III) oxidation capacities of magnetite might be related to the ROS; herein, EPR analysis for both M_0 and M_m was performed in an air atmosphere with DMPO as the radical scavenger. M_0 and M_m presented broad singlet EPR signals, thereby indicating the presence of ROS in both materials (Fig. 6a). Oxygen was trapped by electrons on magnetite surface, producing superoxide radical $O_2^{\cdot-}$ (Eqs. 10–11) (Liu et al., 2015b), and DMPO-$O_2^{\cdot-}$ according to the splitting constant, aN =14.3 G, and the peak signals of 1:1:1:1. In addition, a spectrum of 1:2:2:1 quartet and splitting at aN =aH=14.9 G were observed, which were indicative of the presence of DMPO–OH adduct (Wang et al., 2021a). The $O_2^{\cdot-}$ functioned as an effective oxidizing agent for H_2O and catalyzed the formation of H_2O_2 that further reacted with free electrons to generate ·OH (Eqs. 12–13) (Vandjelovic et al., 2012). Significantly, the signal intensity of DMPO–OH was higher for M_m than for M_0. ·OH and $O_2^{\cdot-}$ were likewise generated by the oxidation of Fe(II) on the magnetite interface via a Fenton-type reaction (Eqs. 14–15) (Perez et al., 2019). After the adsorption of As(III), DMPO-$O_2^{\cdot-}$ and DMPO–OH in M_m intensity decreased (Fig. 6b), hinting the ROS were consumed and involved in As(III) oxidation process (Eq. 12) (Wu et al., 2021). Generally, ·OH and $O_2^{\cdot-}$ might play a vital role in promoting the adsorption of As(III) via oxidization-adsorption mechanism (Eqs. 16–17) (Perez et al., 2019).

$$Fe^{2+} - e^- \rightarrow Fe^{3+} \quad (10)$$

$$O_2 + e^- \rightarrow O_2^{\cdot -} \quad (11)$$

$$O_2^{\cdot -} + 2H_2O - e^- \rightarrow 2H_2O_2 \quad (12)$$

$$H_2O_2 + e^- \rightarrow \cdot OH + OH^- \quad (13)$$

$$Fe^{2+} + O_2 \rightarrow Fe^{3+} + O_2^{\cdot -} \quad (14)$$

$$Fe^{2+} + H_2O_2 \rightarrow Fe^{3+} + \cdot OH + OH^- \quad (15)$$

$$As^{3+} + 2O_2^{\cdot -} \rightarrow As^{5+} + 2O_2^{2-} \quad (16)$$

$$As^{3+} + 2 \cdot OH \rightarrow As^{5+} + 2OH^- \quad (17)$$

EIS patterns were presented in Fig. 6c. In the low frequency region of the electrolyte, as the impedance slope decreased, the rate of ion diffusion between the material and the electrolyte increased. The slopes of M_0 and M_m were 2.92 and 1.71, respectively. The smaller value can be ascribed to large specific surface area and fast electron transfer channels (Lyu et al., 2019). This results validated that the ion storage layers of M_m had relatively higher ion diffusion rates than M_0, suggesting ball milling potentially could accelerate the transfer reactions, therefore facilitating As(III) oxidizing (Zhong et al., 2018). The VSM measurements verified that the As-adsorbed magnetite samples (Fig. S3c–d) exhibited high potential as a magnetically separable adsorbent.

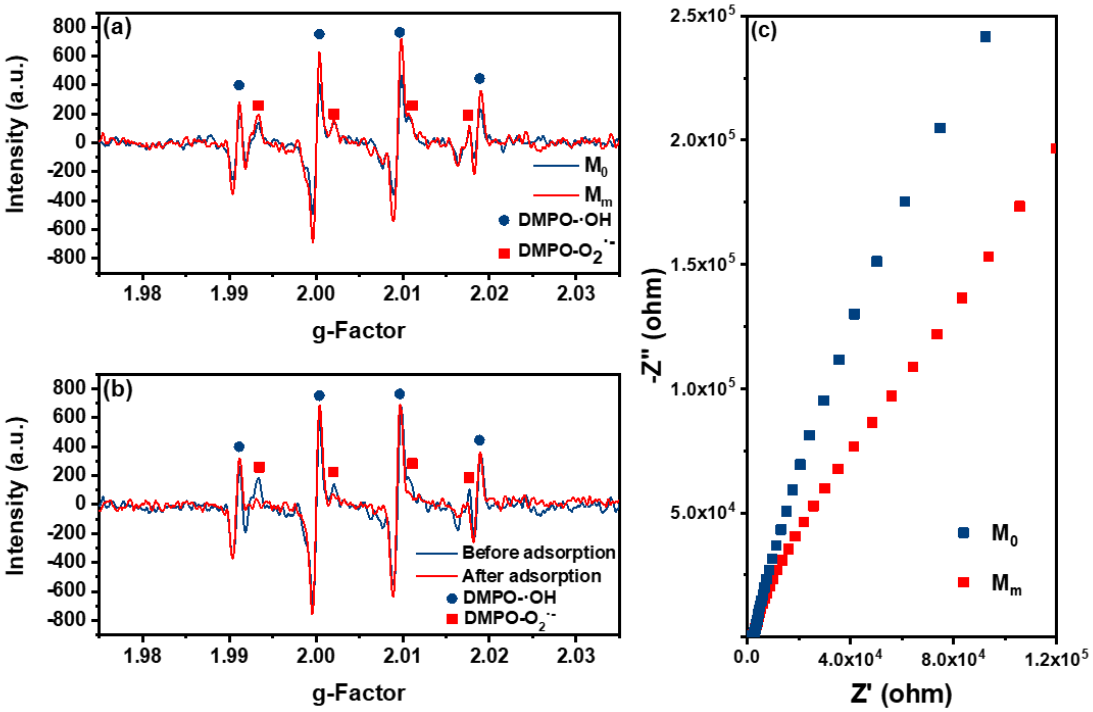

411

412 **Fig. 6** EPR spectra of (a) M_0 and M_m , (b) before and after As(III) adsorption of M_m, and (c) the

413 electrochemical impedance spectra of adsorbents. M_0 and M_m denote natural magnetite and

414 ball-milled magnetite, respectively.

415

416 Plausible mechanisms of As adsorption on M_m are summarized in Fig. 7. The adsorption

417 mechanisms by magnetite adsorbents can be generally interpreted into three parts: 1) Hydrogen

418 bonding. Protonated arsenic interacts with the hydrogen bond acceptor carboxyl group. 2)

419 Surface complexation. The surface complexation between arsenic and surface hydroxyl and

420 carboxyl groups may play a key role in the As(V) and As(III) elimination. 3) Oxidation–

421 adsorption. The As(III) is firstly adsorbed by the mineral adsorptive sites, then oxidized to As(V)

422 via the variation of valence of Fe species, and oxidation effects of ROS ($O_2^{\cdot-}$ and ·OH), which

423 contributes to the improved As(III) adsorption efficiency.

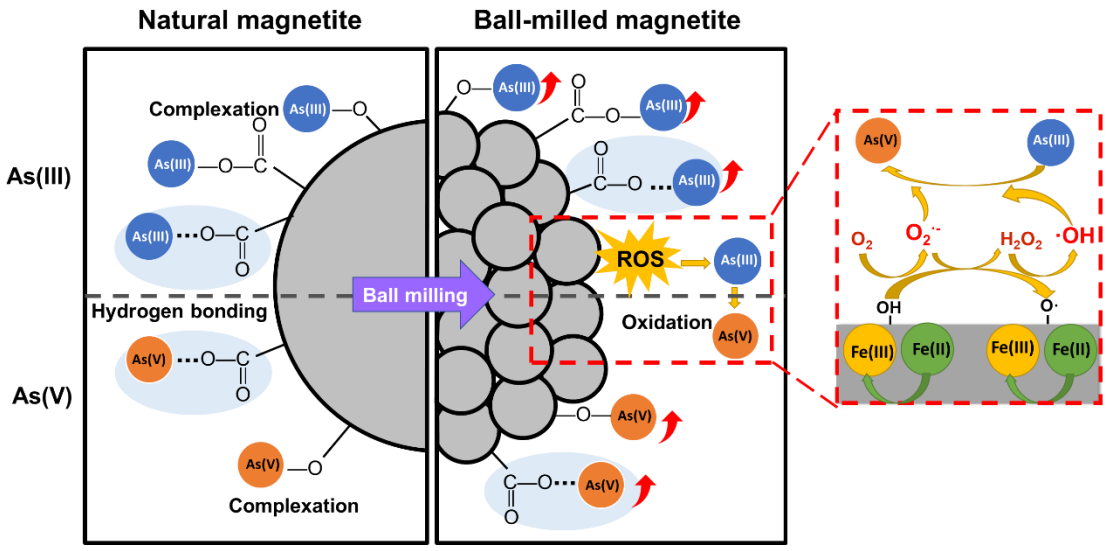

Fig. 7 Mechanisms of As adsorption onto adsorbents. M_0 and M_m denote natural magnetite and ball-milled magnetite, respectively.

3.3 Arsenic stability in the natural and ball-milled magnetite-amended soils

The chemical forms of As in the soil for M_0 and M_m treatments were determined using a five-step sequential extraction method (Fig. 8a). Increasing the application rate of magnetite reduced the exchangeable As, but increased residual fraction of As in the soil. These results demonstrated low leachability/availability of As in amended soils. The 10 wt% dose of exchangeable-As for M_m decreased by 30.25% than the control value (Fig. 8b). Ball milling induced the transformation of magnetite into reactive amorphous Fe (hydr)oxides with high sorption capacities. Furthermore, As could either be adsorbed on the newly formed Fe (hydr)oxides or coprecipitated with the Fe (hydr)oxides. The sizes and specific surface areas of the Fe particles exerted a significant effect on the application of these particles in As stabilization (Komárek et al., 2013).

Arsenic removal depends considerably on the soil pH (Zhang et al., 2010). The soil pH

slightly increased with the presence of different amounts of M_0. The pH ranged from 7.59 to 7.89 that was slightly higher than the pH (7.33) of the control sample (Fig. 8b). Zhang et al. (2010) employed three Fe-containing materials, i.e., nanoscale zerovalent Fe, iron sulfide, and magnetite, for soil treatment, and found an increase in the soil pH by ~0.5 units. This was attributed to the hydrolysis reaction of magnetite in the environment that resulted in the release of OH^- (Wu et al., 2015; Yan et al., 2020a). Unexpectedly, the variation in the dosage of M_m exerted a negligible effect on the soil pH. It was speculated that ball milling induced an increase in the concentration of acidic groups on the material surface, thereby lowering the impact on the soil pH. Soil stabilizers that exert a minimal effect on the soil environment are highly significant in practical applications. The pH of M_m, unlike that of most soil stabilizers, exhibited negligible variation.

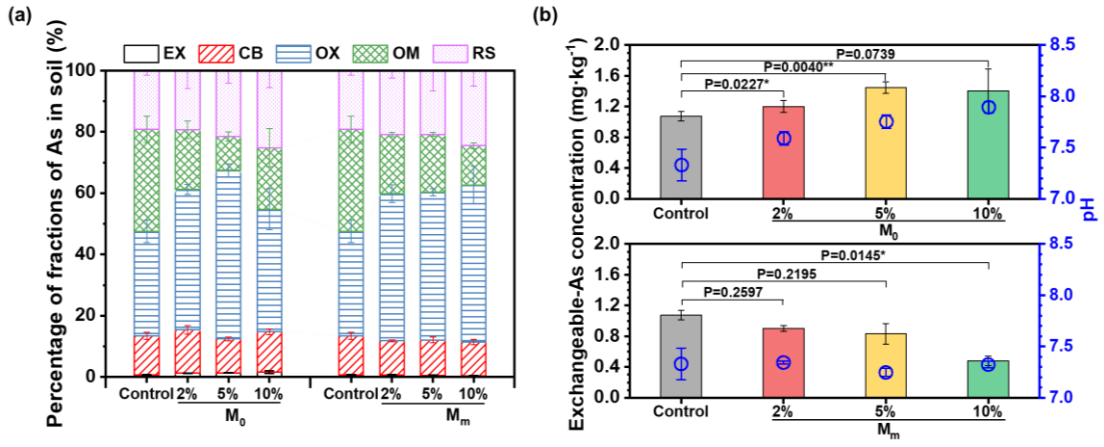

Fig. 8 Concentration profiles of different fractions of As (a); exchangeable-As vs pH (b) in soils after addition of different dosages of natural magnetite (M_0) and ball-milled magnetite (M_m).

3.4 Environmental implications

Extensive research has been conducted on As adsorption by modified Fe-containing materials, and the adsorption capacities of various materials for As(III) and As(V) are summarized in Table S6. The As-adsorption capacity for M_m is comparable to that of other competitive materials. Additionally, ball-milled magnetite resulted in less environmental impacts and stronger redox-suitability, and appeared to be more competitive in practical applications. This cost-effective, easy-to-scale up technology for As removal is suitable for utilization in the low- and low-medium-income countries; furthermore, it can also be extended in many cases for future development of adsorbents.

Ball milling is an effective method for the synthesis of nano-scale magnetite. Ball-milled magnetite facilitates the elimination of As in water and soil systems. This technique allows the rapid and facile fabrication of powerful adsorbents, alleviates the environmental issues originating from the storage of ore waste, and enables waste treatment for sustainable engineering. However, ball milling involves a degree of randomness with the generation of defects and introduction of surface hydroxyl and carboxyl groups and ROS, further efforts are needed to regulate the surface functional groups via electrochemical oxidation, and oxygen plasma treatment etc., to upgrade the natural mineral materials (Bai et al., 2016). Nevertheless, additional investigation should also be conducted to explore the reduction of strong attractive interactions between particles (e.g., coated with a polymer or an inorganic nanostructure) to minimize or avoid particle agglomeration to further enhance its application potential (Favela-Camacho et al., 2019).

4. Conclusions

The present study demonstrated the modification of magnetite via a sustainable, low-cost ball milling process with a mechanistic insight of the absorption of As(III)/As(V) in both aqueous media and soil. The oxidation activity and ability to remove As(III) from water were superior for ball-milled magnetite than for natural magnetite. The coordination of hydroxyl and carboxyl groups in magnetite resulted in the formation of active chemisorption sites for the direct removal of As(III)/As(V). Besides, ball milling not only increased the positive effect of the mineral structure on As(III)/As(V) adsorption but also stimulated Fe(II) oxidation, and surface hydroxyl and carboxyl groups and ROS ($O_2^{\cdot-}$ and ·OH) production to promote As(III) oxidation. Magnetite was easily separated and recovered from the solution after use. Ball-milled magnetite is thus a promising eco-friendly material suitable for the decontamination of As in water and soil via oxidation–adsorption mechanisms. Ball milling exhibits immense potential for maneuvering adsorbents with improved adsorption capacities for various pollutants, thereby facilitating extensive practical applications.

CRediT authorship contribution statement

Xiao Yang: Conceptualization, Writing – review & editing, Methodology. Siyan Liu: Writing – original draft, Data curation, Investigation. Tao Liang: Supervision. Xiulan Yan: Conceptualization, Funding acquisition, Writing – review & editing. Yunhui Zhang: Writing – review & editing. Yaoyu Zhou: Supervision, Writing – review & editing. Binoy Sarkar: Supervision, Writing - review & editing. Yong Sik Ok: Conceptualization, Supervision, Writing – review & editing.

Declaration of Competing Interest

The authors declare that they have no known competing financial interests or personal relationships that could have appeared to influence the work reported in this paper.

Acknowledgements

This study was funded by the National Natural Science Foundation of China (grant number 41571309, U21A2023), a National Research Foundation of Korea (NRF) grant funded by the Korea government (MSIT) (No. 2021R1A2C2011734), and was partly supported by the OJEong Resilience Institute (OJERI) Research Grant from the OJERI, Korea University, Republic of Korea.

Tables

Table 1 Physical and chemical characteristics of the soils

As (mg·kg^{-1})	pH	Organic matter (g·kg^{-1})	Cation-exchange capacity (c mol$^{(+)}$·kg^{-1})	Sandy (%)	Silty (%)	Clay (%)
228.00	7.33	22.88	13.15	67.2	22.0	10.8

513 **Table 2** The physico-chemical properties of natural and ball-milled magnetite

Material	C (%)[a]	H (%)[a]	O (%)[a]	N (%)[a]	S (%)[a]	Particle size (nm)	BET surface area ($m^2 \cdot g^{-1}$)	Total pore volume ($cc \cdot g^{-1}$)	Average pore diameter (nm)
M_0	1.42	0.40	3.85	0.09	0.49	41339	0.75	2.61×10^{-3}	0.14
M_m	1.44	0.75	9.12	0.09	0.61	233	26.00	86.14×10^{-3}	0.13

514 Note: M_0 and M_m denote natural magnetite and ball-milled magnetite, respectively. [a] represent that the element data collected form elemental analyzer (Elementar

515 Analysensysteme GmbH vario EL, Germany)

References

Ahmadzadeh, M., Romero, C., McCloy, J., 2017. Magnetic analysis of commercial hematite, magnetite, and their mixtures. AIP Adv. 8, 056807. https://doi.org/10.1063/1.5006474.

Bai, J., Sun, H., Yin, X., Yin, X., Wang, S., Creamer, A.E., Xu, L., Qin, Z., He, F., Gao, B., 2016. Oxygen-Content-Controllable Graphene Oxide from Electron-Beam-Irradiated Graphite: Synthesis, Characterization, and Removal of Aqueous Lead [Pb(II)]. ACS Appl. Mater. Interfaces 8, 38, 25289–25296. https://doi.org/10.1021/acsami.6b08059.

Bhardwaj, A., Rajput, R., Misra, K., 2019. Status of arsenic remediation in India, in: S. Ahuja (Ed.), Advances in Water Purification Techniques, Elsevier, New Caledonia, pp. 219–258. https://doi.org/10.1016/B978-0-12-814790-0.00009-0.

Byrne, J.M., Van der Laan, G., Figueroa, A.I., Qafoku, O., Wang, C., Pearce, C.I., Jackson, M., Feinberg, J., Rosso, K.M., Kappler, A., 2016. Size-dependent microbial oxidation and reduction of magnetite nano and microparticles. Sci. Rep. 6, 30969. https://doi.org/10.1038/srep30969.

Chen, H., Xu, F., Chen, Z., Jiang, O., Gustave, W., Tang, X., 2020. Arsenic and cadmium removal from water by a calcium-modified and starch-stabilized ferromanganese binary oxide. J. Environ. Sci. 96, 186–193. https://doi.org/10.1016/j.jes.2020.03.060.

Dutta, S., Manna, K., Srivastava, S.K., Gupta, A.K., Yadav, M.K., 2020. Hollow polyaniline microsphere/Fe3O4 nanocomposite as an effective adsorbent for removal of arsenic from water. Sci. Rep. 10, 4982. https://doi.org/10.1038/s41598-020-61763-z.

Ellis, A.B., Geselbracht, M.J., Johnson, B.J., Lisensky, G.C., Robinson, W.R., 1993. Teaching General Chemistry: A Material Science Companion, American Chemical Society, Washington DC.

Favela-Camacho, S.E., Samaniego-Benítez, E.J., Godínez-García, A., Avilés-Arellano, L.M., Pérez-Robles, J.F.,2019. How to decrease the agglomeration of magnetite nanoparticles and increase their stability using surface properties. Colloid Surf. A-Physicochem. Eng. Asp. 574, 29-35. https://doi.org/10.1016/j.colsurfa.2019.04.016.

Hao, L., Liu, M., Wang, N., Li, G., 2018. A critical review on arsenic removal from water

using iron-based adsorbents. RSC Adv. 8, 39545–39560. https://doi.org/10.1039/C8RA08512A.

Khalid, S., Shahid, M., Niazi, N.K., Murtaza, B., Bibi, I., Dumat, C., 2017. A comparison of technologies for remediation of heavy metal contaminated soils. J. Geochem. Explor. 182, 247–268. https://doi.org/10.1016/j.gexplo.2016.11.021.

Komárek, M., Vaněk, A., Ettler, V., 2013. Chemical stabilization of metals and arsenic in contaminated soils using oxides – A review, Environ. Pollut. 172, 9–22. https://doi.org/10.1016/j.envpol.2012.07.045.

Kumar, M., Xiong, X., Wan, Z., Sun, Y., Tsang, D.C.W., Gupta, J., Gao, B., Cao, X., Tang, J., Ok, Y.S., 2020. Ball milling as a mechanochemical technology for fabrication of novel biochar nanomaterials. Bioresource Technol. 312, 123613. https://doi.org/10.1016/j.biortech.2020.123613.

Lai, Z., Chen, Q., 2017. Characterization and discrete element simulation of grading and shape-dependent behavior of JSC-1A Martian regolith simulant. Granul. Matter. 19, 69. https://doi.org/10.1007/s10035-017-0754-1.

Largitte, L., Pasquier, R., 2016. A review of the kinetics adsorption models and their application to the adsorption of lead by an activated carbon, Chem. Eng. Res. Des. 109, 495–504. https://doi.org/10.1016/j.cherd.2016.02.006.

Liu, A., Liu, J., Pan, B., Zhang, W., 2014. Formation of lepidocrocite (γ-FeOOH) from oxidation of nanoscale zerovalent iron (nZVI) in oxygenated water, RSC Adv. 4, 57377–57382. https://doi.org/10.1039/C4RA08988J.

Liu, A.H., Yu, B., He, L.N., 2015a. Catalytic conversion of carbon dioxide to carboxylic acid derivatives. Greenhouse Gas Sci. Technol. 5: 17-33. https://doi.org/10.1002/ghg.1461.

Liu, C., Chuang, Y., Chen, T., Tian, Y., Li, H., Wang, M., Zhang, W., 2015b. Mechanism of arsenic adsorption on magnetite nanoparticles from water: Thermodynamic and spectroscopic studies, Environ. Sci. Technol. 49, 7726–7734. https://doi.org/10.1021/acs.est.5b00381.

Liu, G., Fernandez, A., Cai, Y., 2011. Complexation of arsenite with humic acid in the presence of ferric iron, Environ. Sci. Technol. 45, 3210–3216. https://doi.org/10.1021/es102931p.

573 Lyu, H., Yu, Z., Gao, B., He F., Huang, J., Tang, J., Shen, B., 2019. Ball-milled biochar for
574 alternative carbon electrode. Environ. Sci. Pollut. Res. 26, 14693–14702.
575 https://doi.org/10.1007/s11356-019-04899-4
576 Ma, L., Cai, D.M., Tu, S.X., 2020. Arsenite simultaneous sorption and oxidation by natural
577 ferruginous manganese ores with various ratios of Mn/Fe. Chem. Eng. J. 382, 123040.
578 https://doi.org/10.1016/j.cej.2019.123040.
579 Matović, L.L., Vukelić, N.S., Jovanović, U.D., Kumrić, K.R., Krstić, J.B., Babić, B.M.,
580 Đukić, A.B., 2019. Mechanochemically improved surface properties of activated carbon cloth
581 for the removal of As(V) from aqueous solutions. Arab. J. Chem. 12, 4446–4457.
582 https://doi.org/10.1016/j.arabjc.2016.07.004.
583 Medina, B., Verdério Fressati, M.G., Gonçalves, J.M., Bezerra, F.M., Pereira Scacchetti,
584 F.A., Moisés, M.P., Bail, A., Samulewski, R.B., 2019. Solventless preparation of Fe_3O_4 and
585 Co_3O_4 nanoparticles: A mechanochemical approach. Mater. Chem. Phys. 226, 318–322.
586 https://doi.org/10.1016/j.matchemphys.2019.01.043.
587 Mendili, Y.E., Bardeau, J.F., Randrianantoandro, N., Greneche, J.M., Grasset, F., 2016.
588 Structural behavior of laser-irradiated gamma- Fe_2O_3 nanocrystals dispersed in porous silica
589 matrix: gamma-Fe_2O_3 to alpha- Fe_2O_3 phase transition and formation of epsilon- Fe2O3. Sci.
590 Technol. Adv. Mat. 17, 597-609. http://dx.doi.org/10.1080/14686996.2016.1222494.
591 Miretzky, P., Cirelli, A.F., 2010. Remediation of arsenic-contaminated soils by iron
592 amendments: A Review. Crit. Rev. Environ. Sci. Technol. 40, 93-115.
593 https://doi.org/10.1080/10643380802202059.
594 Mora–Mendoza, E.Y., Sarmiento Santos, A., Vera López, E., Drozd, V., Durygin, A.,
595 Chen, J., Saxena, S.K., 2019. Siderite Formation by Mechanochemical and High Pressure–High
596 Temperature Processes for CO_2 Capture Using Iron Ore as the Initial Sorbent. Processes 7(10).
597 https://doi.org/10.3390/pr7100735.
598 Moon, J.W., Rawn, C.J., Rondinone, A.J., Wang, W., Vali, H., Yeary, L.W., Love, L.J.,
599 Kirkham, M.J., Gu, B., Phelps, T.J., 2010. Crystallite sizes and lattice parameters of
600 nanobiomagnetite particles. J. Nanosci. Nanotechnol. 10, 8298–8306.
601 https://doi.org/10.1166/jnn.2010.2745.

Nandiyanto, A.B.D., Zaen, R., Oktiani, R., 2018. Working volume in high-energy ball-milling process on breakage characteristics and adsorption performance of rice straw ash. Arab. J. Sci. Eng. 43, 6057–6066. https://doi.org/10.1007/s13369-018-3265-4.

Peng, Q.S., Zhao, H.Y., Qian, L., Wang, Y.B., Zhao, G.H., 2015. Design of a neutral photo-electro-Fenton system with 3D-ordered macroporous Fe_2O_3/carbon aerogel cathode: High activity and low energy consumption, Appl. Catal., B 174, 157–166. https://doi.org/10.1016/j.apcatb.2015.02.031.

Peng,Y., Tang, H., Yao, B., Gao, X., Yang, X., Zhou, Y., 2021. Activation of peroxymonosulfate (PMS) by spinel ferrite and their composites in degradation of organic pollutants: A Review. J. Chem. Eng. 414, 128800. https://doi.org/10.1016/j.cej.2021.128800.

Perez, J.P.H., Tobler, D.J., Thomas, A.N., Freeman, H.M., Dideriksen, K., Radnik, J., Benning, L.G., 2019. Adsorption and reduction of arsenate during the Fe^{2+}-induced transformation of ferrihydrite, ACS Earth Space Chem. 3, 884–894. https://doi.org/10.1021/acsearthspacechem.9b00031.

Petrovský, E., Alcalá, M.D., Criado, J.M., Grygar, T., Kapička, A., Šubrt, J., 2000. Magnetic properties of magnetite prepared by ball milling of hematite with iron. J. Magn. Mater. 210, 257–273. https://doi.org/10.1016/S0304-8853(99)00624-1.

Pholosi, A., Naidoo,E.B., Ofomaja, A.E., 2020. Intraparticle diffusion of Cr(VI) through biomass and magnetite coated biomass: A comparative kinetic and diffusion study. South African J. Chem. Eng. 32, 39-55. https://doi.org/10.1016/j.sajce.2020.01.005.

Salem, N.M., Awwad, A.M., 2013. A novel approach for synthesis magnetite nanoparticles at ambient temperature, J. Nanosci. Nanotechnol. 3, 35–39. https://doi.org/10.5923/j.nn.20130303.01.

Samimi, S., Maghsoudnia, N., Eftekhari, R.B., Dorkoosh, F., 2019. Lipid-based nanoparticles for drug delivery systems, in: S.S. Mohapatra, S. Ranjan, N. Dasgupta, R.K. Mishra, S. Thomas (Eds.), Characterization and Biology of Nanomaterials for Drug Delivery, Elsevier, pp. 47–76. https://doi.org/10.1016/B978-0-12-814031-4.00003-9.

Schaefer, M.V., Gorski, C.A., Scherer, M.M., 2011. Spectroscopic evidence for interfacial Fe(II)−Fe(III) electron transfer in a clay mineral, Environ. Sci. Technol. 45, 540–545.

https://doi.org/10.1021/es102560m.

Shankar, S., Shanker, U., Shikha, 2014. Arsenic contamination of groundwater: A review of sources, prevalence, health risks, and strategies for mitigation. Sci. World J. 2014, 304524. https://doi.org/10.1155/2014/304524.

Shebanova, O.N., Lazor, P., 2003. Raman spectroscopic study of magnetite ($FeFe_2O_4$): A new assignment for the vibrational spectrum. J. Solid State Chem. 174, 424–430. https://doi.org/10.1016/S0022-4596(03)00294-9.

Shen, X., Guo, X., Zhang, M., Tao, S., Wang, X., 2015. Sorption mechanisms of organic compounds by carbonaceous materials: Site energy distribution consideration. Environ. Sci. Technol. 49, 4894–4902. https://doi.org/10.1021/es506034e.

Silva, G.C., Vasconcelos, I.F., de Carvalho, R.P., Dantas, M.S.S., Ciminelli, V.S.T., 20019. Molecular modeling of iron and arsenic interactions with carboxy groups in natural biomass, Environ. Chem. 6, 350–356. https://doi.org/10.1071/EN09031.

Singh, S.K., Townsend, T.G., Mazyck, D., Boyer, T.H., 2012. Equilibrium and intraparticle diffusion of stabilized landfill leachate onto micro and mesoporous activated carbon, Water Res. 46, 491–499. https://doi.org/10.1016/j.watres.2011.11.007.

Srivastava, M., Alla, S.K., Meena, S.S., Gupta, N., Mandal, R.K., Prasad, N.K., 2018. $ZnxFe_{3-x}O_4$ ($0.01 \leq x \leq 0.8$) nanoparticles for controlled magnetic hyperthermia application. New J. Chem. 42, 7144–7153. https://doi.org/10.1039/C8NJ00547H.

Su, C., 2017. Environmental implications and applications of engineered nanoscale magnetite and its hybrid nanocomposites: A review of recent literature. J. Hazard. Mater. 322, 48–84. https://doi.org/10.1016/j.jhazmat.2016.06.060.

Tung, H., Huang, J., Tsai, D., Ai, C., Yu, G., 2009. Hardness and residual stress in nanocrystalline ZrN films: Effect of bias voltage and heat treatment. Mater. Sci. Eng. A 500, 104–108. https://doi.org/10.1016/j.msea.2008.09.006.

Turunen, K., Backnäs, S., Neitola, R., Pasanen, A., 2016. Factors controlling the migration of tailings-derived arsenic: A case study at the Yara Siilinjärvi site. Mine Water Environ. 35, 407–420. https://doi.org/10.1007/s10230-016-0393-5.

Vandjelovic, N., Zhu, H., Misra, H.P., Zimmerman, R.P., Jia, Z., Li, Y., 2012. EPR studies

660 on hydroxyl radical-scavenging activities of pravastatin and fluvastatin, Mol. Cell Biochem.
661 364, 71–77. https://doi.org/10.1007/s11010-011-1206-6.
662 Veloso, C.H., Filippov, L.O., Filippova, I.V., Ouvrard, S., Araujo, A.C., 2020. Adsorption
663 of polymers onto iron oxides: Equilibrium isotherms. J. Mater. Res. Technol. 9, 779–788.
664 https://doi.org/10.1016/j.jmrt.2019.11.018.
665 Vikrant, K., Kim, K.-H., Ok, Y.S., Tsang, D.C.W., Tsang, Y.F., Giri, B.S., Singh, R.S., 2018.
666 Engineered/designer biochar for the removal of phosphate in water and wastewater. Sci. Total
667 Environ. 616, 617, 1242–1260. https://doi.org/10.1016/j.scitotenv.2017.10.193.
668 Vithanage, M., Herath, I., Joseph, S., Bundschuh, J., Bolan, N., Ok, Y.S., Kirkham, M.B.,
669 Rinklebe, J., 2017. Interaction of arsenic with biochar in soil and water: A critical review.
670 Carbon 113, 219-230. https://doi.org/10.1016/j.carbon.2016.11.032.
671 Wang, L., Chen, T., Cui, J., Liu, W., 2020. Study on magnetic difference of artificial
672 magnetite and natural magnetite. J. Phys.: Conf. Ser. 1699, 012040.
673 https://doi.org/10.1088/1742-6596/1699/1/012040.
674 Wang, L., Lan, X., Peng, W., Wang, Z., 2021a. Uncertainty and misinterpretation over
675 identification, quantification, and transformation of reactive species generated in catalytic
676 oxidation processes: A review. J. Hazard. Mater. 408, 124436.
677 https://doi.org/10.1016/j.jhazmat.2020.124436.
678 Wang, L., Ok, Y.S., Tsang, D.C.W., Alessi, D.S., Rinklebe, J., Mašek, O., Bolan, N.S., Hou,
679 D., 2021b. Biochar composites: Emerging trends, field successes and sustainability
680 implications. Soil Use Manage. 00, 1–25. https://doi.org/10.1111/sum.12731.
681 Wang, Y., Li, B., Zhou, Y., Jia, D., 2009. In situ mineralization of magnetite nanoparticles
682 in chitosan hydrogel. Nanoscale Res. Lett. 4, 1041. https://doi.org/10.1007/s11671-009-9355-
683 1.
684 Wenzel, W.W., Kirchbaumer, N., Prohaska, T., Stingeder, G., Lombi, E., Adriano, D.C.,
685 2001. Arsenic fractionation in soils using an improved sequential extraction procedure, Anal.
686 Chim. Acta. 436, 309–323. https://doi.org/10.1016/S0003-2670(01)00924-2.
687 Wojciechowska, A., Lendzion-Bieluń, Z., 2020. Synthesis and characterization of
688 magnetic nanomaterials with adsorptive properties of arsenic ions. Molecules 25, 4117.

https://doi.org/10.3390/molecules25184117.

World Health Organization, Guidelines for Drinking-Water Quality, second ed. Geneva, 1993.

Wu, B., Wan, J., Zhang, Y., Pan, B., Lo, I.M.C., 2020. Selective phosphate removal from water and wastewater using sorption: Process fundamentals and removal mechanisms, Environ. Sci. Technol. 54, 50–66. https://doi.org/10.1021/acs.est.9b05569.

Wu, K., Wang, M., Li, A., Zhao, Z., Liu, T., Hao, X., Yang, S., Jin, P., 2021. The enhanced As(III) removal by Fe–Mn–Cu ternary oxide via synergistic oxidation: Performances and mechanisms. Chem. Eng. J. 406, 126739. https://doi.org/10.1016/j.cej.2020.126739.

Wu, W., Wu, Z., Yu, T., Jiang, C., Kim, W.S., 2015. Recent progress on magnetic iron oxide nanoparticles: Synthesis, surface functional strategies, and biomedical applications. Sci. Technol. Adv. Mater. 16, 023501. https://doi.org/10.1088/1468-6996/16/2/023501.

Xie, F., Wu, F., Liu, G., Mu, Y., Feng, C., Wang, H., Giesy, J.P., 2014. Removal of phosphate from eutrophic lakes through adsorption by in situ formation of magnesium hydroxide from diatomite, Environ. Sci. Technol. 48, 582–590. https://doi.org/10.1021/es4037379.

Xu, X., Xu, Z., Huang, J., Gao, B., Zhao, L., Qiu, H., Cao, X., 2021. Sorption of reactive red by biochars ball milled in different atmospheres: Co-effect of surface morphology and functional groups. Chem. Eng. J. 413, 127468. https://doi.org/10.1016/j.cej.2020.127468.

Yan, X., Shao, J., Wen, Q. Shen, J., 2020a. Stabilization of soil arsenic by natural limonite after mechanical activation and the associated mechanisms. Sci. Total Environ. 708, 135118. https://doi.org/10.1016/j.scitotenv.2019.135118.

Yan, X., Zhao, W., Yang, X., Liu, C., Zhou, Y., 2020b. Input–output balance of cadmium in typical agriculture soils with historical sewage irrigation in China. J. Environ. Manage. 276, 111298. https://doi.org/10.1016/j.jenvman.2020.111298.

Yang, X., Li, J., Liang, T., Yan, X., Zhong, L., Shao, J., El-Naggar, A., Guan, C.Y., Liu, J., Zhou, Y., 2021. A combined management scheme to simultaneously mitigate As and Cd concentrations in rice cultivated in contaminated paddy soil. J. Hazard. Mater. 416, 125837. https://doi.org/10.1016/j.jhazmat.2021.125837.

718 Yuan, K., Lee, S.S., Cha, W., Ulvestad, A., Kim, H., Abdilla, B., Sturchio, N.C., Fenter, P.,
719 2019. Oxidation-induced strain and defects in magnetite crystals. Nat. Commun. 10, 703.
720 https://doi.org/10.1038/s41467-019-08470-0.
721 Zhang, B., Zhang, T., Zhang, Z., Xie, M., 2019. Hydrothermal synthesis of a
722 graphene/magnetite/montmorillonite nanocomposite and its ultrasonically assisted methylene
723 blue adsorption, J. Mater. Sci. 54, 11037–11055. https://doi.org/10.1007/s10853-019-03659-6.
724 Zhang, L., Qin, X., Tang, J., Liu, W., Yang, H., 2017. Review of arsenic geochemical
725 characteristics and its significance on arsenic pollution studies in karst groundwater. Southwest
726 China, Appl. Geochem. 77, 80–88. https://doi.org/10.1016/j.apgeochem.2016.05.014.
727 Zhang, M., Wang, Y., Zhao, D., Pan, G., 2010. Immobilization of arsenic in soils by
728 stabilized nanoscale zerovalent iron, iron sulfide (FeS), and magnetite (Fe_3O_4) particles, Chin.
729 Sci. Bull. 55, 365–372. https://doi.org/10.1007/s11434-009-0703-4.
730 Zhang, X., Chu, Y., Zhang, H., Hu, J., Wu, F., Wu, X., Shen, G., Yang, Y., Wang, B., Wang,
731 X., 2021. A mechanistic study on removal efficiency of four antibiotics by animal and plant
732 origin precursors-derived biochars. Sci. Total Environ. 772, 145468.
733 https://doi.org/10.1016/j.scitotenv.2021.145468.
734 Zheng, Q., Tu, S., Hou, J., Ni, C., Wang, M., Ren, L., Wang, M., Cao, M., Xiong, S., Tan,
735 W., 2021. Insights into the underlying mechanisms of stability working for As(III) removal by
736 Fe-Mn binary oxide as a highly efficient adsorbent. Water Res. 203, 117558.
737 https://doi.org/10.1016/j.watres.2021.117558
738 Zhong, D., Ren, S., Dong, X., Yang, X., Wang, L., Chen, J., Zhao, Z., Zhang, Y., Tsang,
739 D.C.W., Crittenden, J.C., 2021. Rice husk-derived biochar can aggravate arsenic mobility in
740 ferrous-rich groundwater during oxygenation. Water Res. 200, 117264.
741 https://doi.org/10.1016/j.watres.2021.117264.
742 Zhong, D., Zhang, Y., Wang, L., Chen, J., Jiang, Y., Tsang, D.C.W., Zhao, Z., Ren, S., Liu,
743 Z., Crittenden, J.C., 2018. Mechanistic insights into adsorption and reduction of hexavalent
744 chromium from water using magnetic biochar composite: Key roles of Fe3O4 and persistent
745 free radicals, Environ. Pollut. 243, 1302-1309. https://doi.org/10.1016/j.envpol.2018.08.093.
746

747 Supplementary Information for:

748 **Ball-milled magnetite for efficient arsenic decontamination:**

749 **Insights into oxidation–adsorption mechanism**

750

751 **Xiao Yang[a], Siyan Liu[a,b], Tao Liang[a,b], Xiulan Yan[a,*], Yunhui Zhang[c], Yaoyu Zhou[d],**

752 **Binoy Sarkar[e], Yong Sik Ok[f,**]**

753

754 [a] Key Laboratory of Land Surface Pattern and Simulation, Institute of Geographic Sciences

755 and Natural Resources Research, Chinese Academy of Sciences, Beijing 100101, China

756 [b] College of Resources and Environment, University of Chinese Academy of Sciences,

757 Beijing 100190, China

758 [c] College of Environmental Science and Engineering, Tongji University, Shanghai, 200092,

759 China

760 [d] College of Resources and Environment, Hunan Agricultural University, Changsha,

761 410128, China

762 [e] Lancaster Environment Centre, Lancaster University, Lancaster, LA1 4YQ, United

763 Kingdom

764 [f] Korea Biochar Research Center, O-Jeong Eco-Resilience Institute (OJERI) & Division

765 of Environmental Science and Ecological Engineering, Korea University, Seoul 02841,

766 Republic of Korea

Supplementary material

The SI includes 3 texts, 6 tables and 3 figures. Detailed explanations for materials characterization, batch adsorption experiment, and kinetics and isotherm modelling as well as corresponding calculations were also provided here.

Text S1

Magnetite was subjected to particle size analysis (Mastersizer 2000, Malvern Panalytical, Worcestershire, UK) via analyzing a suspension 200 $mg \cdot L^{-1}$ particles in water. The morphological and compositional features of the samples were characterized via scanning electron microscopy (SEM) combined with energy-dispersive X-ray spectroscopy (SEM-EDS, MIRA 3LM, Tescan, Czechia). The specific surface area and pore size were measured via Brunauer–Emmett–Teller (BET) method (BSD-PS1/2, Beishide Instrument, China). The specific surface area, pore-volume, and pore size of the magnetite were assessed by N_2 adsorption-desorption isotherm analysis at 77 K using a volumetric adsorption analyzer (BSD-PS1/2, Beishide Instrument, China). Prior to each measurement of textural properties, the samples were degassed under vacuum (10 μmHg) at a temperature of 473 K for 2 h. Specific surface areas were calculated using the Brunauer Emmett Teller (BET) method from adsorption data obtained in the relative pressure (P/P_0) range of 0.01–0.1. The total pore volumes were obtained using the amount of N_2 adsorbed at a relative pressure of 0.99. The C, H, N, S, O elemental were analyzed via elemental analyzer (Elementar Analysensysteme GmbH vario EL, Germany).

Raman spectroscopy (LabRAM HR Evolution, HORIBA Ltd., Jobin-Yvon, France) was performed using the 514 nm line of an Ar^+ laser. The surface functionalities of the samples were characterized using X-ray photoelectron spectroscopy (XPS; Axis Ultra, Kratos Analytical Ltd., Manchester, England). Fourier-transform infrared (FTIR) spectroscopy (Hyperion Tensor 37, Germany) was detected, and dewatered the samples at 105 ℃ for 8 hours before analysis. The collected spectra were baselined using OMNIC software 6.0 (Thermo-Nicolet). The O–Si–O

795 combination bands at 1639 cm^{-1} was taken as the basis for normalization (Krivoshein
796 et al., 2020). For normalization, the absorbance value of this band was set to 1.0 and
797 the complete spectrum was multiplied by a ratio factor. The normalization is based on
798 the equation below:

$$a_{norm}(w) = a(w) \cdot \frac{1}{a(1639\ cm^{-1})} \quad (1)$$

799 where $a_{norm}(w)$ is normalized absorbance spectrum as a function of wave number
800 w; $a(w)$ is original absorbance spectrum; $a(1639\ cm^{-1})$ is original absorbance value at
801 the reference band at wave number 1639 cm^{-1}.

802 The structural features and crystal forms of samples were investigated by using X-ray
803 diffraction (XRD, D/max-rA, Rigaku Corporation, Tokyo, Japan) patterns with monochromatic
804 Cu Ka radiation (k = 0.154 nm). The XRD patterns were processed using MDI Jade 6.5 loaded
805 with the inorganic crystal structure database (ICSD; Materials Data Inc., California, America).
806 The crystallite size of natural magnetite was calculated based on the datasets using Scherrer's
807 formula expressed as follows (Rajendrachari et al., 2020):

$$D = \frac{K\lambda}{\beta cos\theta} \quad (2)$$

808 where D is the average crystallite size (nm), K is a constant equal to 0.94, λ is the
809 wavelength of X-ray radiation (0.154 nm), β is the full-width half maximum (FWHM) of the
810 high-intensity peak (in radians), and 2θ is the Bragg's angle (°).

811 The zeta potential (ζ) and the hydrodynamic radius of samples were analyzed using a zeta
812 potential measurement system (Zetasizer Nano ZSP, Malvern Panalytical, Worcestershire, UK).
813 The magnetic properties were evaluated using vibrating sample magnetometry (VSM,
814 PMC3900, Lakeshore Cryotronics, Westerville, USA) at around 298 K.

815 The generation of ROS in the materials was detected via electron paramagnetic resonance
816 (EPR, Bruker, Germany). Briefly, dimethyl pyridine N-oxide (DMPO) was used as a spin-
817 trapping agent because it could react with ·OH or $\cdot O^{2-}$ to produce the signals of the DMPO-·OH
818 adducts and DMPO-$O_2^{\cdot-}$ adducts, respectively. The conductivities of M_0 and M_m were evaluated
819 by measuring the electrochemical impedance spectra (EIS, CS310, CorrTest, China) according
820 to previous study (Zhong et al., 2018).

821

822 **Text S2**

823 Batch experiments were performed to evaluate the As-adsorption capacities of M_0 and M_m.
824 Disodium hydrogen arsenate ($Na_2HAsO_4 \cdot 7H_2O$) and sodium arsenite ($NaAsO_2$) were used for
825 preparation of the stock solution of As(III) and As(V). Sodium nitrate ($NaNO_3$, 0.01 M) was
826 employed as a background electrolyte to regulate the ionic strength, and the pH of the mixture
827 was adjusted to 7.0 using HNO_3 (1 M, 0.1 M) and/or NaOH (1 M, 0.1 M).

828 Kinetic studies were conducted at a fixed As(III) or As(V) concentration (10 $mg \cdot L^{-1}$) by
829 interacting 50 mL of solution with M_0 and M_m (2 $g \cdot L^{-1}$). This was followed by 70 h of agitation
830 at 25 °C and samples withdrawn at specified time intervals. The adsorption isotherm
831 experiments were conducted via addition of 2 $g \cdot L^{-1}$ of the adsorbent to 25 mL of the As(III) or
832 As(V) solution with initial As concentrations of 5–100 $mg \cdot L^{-1}$. The mixture was filtered after
833 24 h of adsorption. The As concentration in the supernatant was determined using atomic
834 fluorescence spectrometry (AFS; AFS-9780, Haiguang Instrument Equipment Co. Ltd., Beijing,
835 China) with a detection limit of 0.01 $\mu g \cdot L^{-1}$. The adsorption capacities of As(III) and/or As(V)
836 on M_0 and M_m were calculated as follows:

$$Q_t(or\ Q_e) = \frac{V}{m} \times (C_0 - C_t(or\ C_e)), \quad (3)$$

837 where Q_t and Q_e are the adsorption capacity per gram dry weight of the adsorbents at a
838 specific time and at equilibrium ($mg \cdot g^{-1}$), respectively; C_0 denotes the initial concentration of
839 As(III) and As(V); C_t ($mg \cdot L^{-1}$) signifies the concentration of As(III) or As(V) at a certain
840 sampling time; and C_e ($mg \cdot L^{-1}$) represents the final concentration of As(III) or As(V).
841 Furthermore, V (L) is the volume of the As(III) and As(V) solutions, and m (g) is the mass of

842 the adsorbent.

843

844 **Text S3**

845 The adsorption kinetic data were fitted using the pseudo-first-order, pseudo-second-order,
846 Elovich, and Weber–Morris models (Table S2). This enables the elucidation of adsorption
847 mechanisms and determination of the rate processes and kinetic parameters. The pseudo-first-
848 and pseudo-second-order models are empirical kinetic models and used to describe the
849 adsorption process based on chemical reaction kinetics (Largitte et al., 2016). The Elovich
850 model has proven to be suitable for highly heterogeneous systems (Wu et al., 2009). The first
851 three models belong to the empirical formula for surface adsorption (Zhang et al., 2018). The
852 Weber–Morris model (intraparticle diffusion model) is of major interest because internal
853 diffusion determines the adsorption rate in most liquid systems (Zhang et al., 2018).

854 Adsorption isotherm models describe the mobility of the adsorbate from the aqueous phase
855 to the solid phase at a constant temperature (Largitte et al., 2016). The Langmuir, Freundlich,
856 Temkin, and Dubinin–Radushkevich models were used to obtain the adsorption isotherms, as
857 presented in Table S3. The Freundlich isotherm is suitable for nonideal adsorption on
858 heterogeneous surfaces. It is assumed that there are multiple types of available sites, each with
859 different free energy of adsorption, acting simultaneously (Singh et al., 2012). The Langmuir
860 model is adopted for ideal solutions and for homogeneous and independent monolayer
861 adsorption. The Temkin model assumes that adsorption is a multilayer process (Al-Ghouti and
862 Da'ana, 2020). The Dubinin–Radushkevich model aims to distinguish between the physical and
863 chemical adsorptions of ions (Al-Ghouti and Da'ana, 2020).

864

References

Al-Ghouti, M.A., Da'ana, D.A., 2020. Guidelines for the use and interpretation of adsorption isotherm models: A review. J. Hazard. Mater. 393, 122383. https://doi.org/10.1016/j.jhazmat.2020.122383.

Krivoshein, P.K., Volkov, D.S., Rogova, O.B., Proskurnin, M.A., 2020. FTIR photoacoustic spectroscopy for identification and assessment of soil components: Chernozems and their size fractions. Photoacoustics 18, 100162. https://doi.org/10.1016/j.pacs.2020.100162.

Largitte, L., Pasquier, R., 2016. A review of the kinetics adsorption models and their application to the adsorption of lead by an activated carbon, Chem. Eng. Res. Des. 109, 495–504. https://doi.org/10.1016/j.cherd.2016.02.006.

Rajendrachari, S., Karaoglanli, A.C., Ceylan, Y., Uzun, O., 2020. A fast and robust approach for the green synthesis of spherical magnetite (Fe_3O_4) nanoparticles by *Tilia tomentosa* (Ihlamur) leaves and its antibacterial studies, Pharm. Sci. 26, 175–183. https://doi.org/10.34172/ps.2020.5.

Singh, S.K., Townsend, T.G., Mazyck, D., Boyer, T.H., 2012. Equilibrium and intraparticle diffusion of stabilized landfill leachate onto micro and mesoporous activated carbon, Water Res. 46, 491–499. https://doi.org/10.1016/j.watres.2011.11.007.

Wu, F., Tseng, R., Juang, R., 2009. Characteristics of Elovich equation used for the analysis of adsorption kinetics in dye–chitosan systems, Chem. Eng. J. 150, 366–373. https://doi.org/10.1016/j.cej.2009.01.014.

Zhang, Y., Jin, F., Shen, Z., Lynch, R., Al-Tabbaa, A., 2018. Kinetic and equilibrium modelling of MTBE (methyl tert-butyl ether) adsorption on ZSM-5 zeolite: Batch and column studies. J. Hazard. Mater. 347, 461–469. https://doi.org/10.1016/j.jhazmat.2018.01.007.

Zhong, D., Zhang, Y., Wang, L., Chen, J., Jiang, Y., Tsang, D.C.W., Zhao, Z., Ren, S., Liu, Z., Crittenden, J.C., 2018. Mechanistic insights into adsorption and reduction of hexavalent chromium from water using magnetic biochar composite: Key roles of Fe3O4 and persistent free radicals, Environ. Pollut. 243, 1302-1309. https://doi.org/https://doi.org/10.1016/j.envpol.2018.08.093.

893 **Table S1** Chemical compositions of the natural magnetite (wt.%)

Components	**TFe**	**SiO_2**	**CaO**	**MgO**	**MnO**	**TiO_2**	**Al_2O_3**	**SO_3**	**Cl**	**K_2O**	**Cr_2O_3**	**V_2O_3**	**BaO**	**NiO**	**ZnO**	**PbO**
Content	64.93	1.25	1.04	0.56	0.37	0.36	0.36	0.18	0.13	0.11	0.09	0.06	0.04	0.01	0.01	0.01

894 Chemical compositions of the magnetite samples measured by XRF (Niton XL3t 950).

895

Table S2 Adsorption kinetic models

Model	Model equation	Model parameters
Pseudo-first-order	$\ln(Q_e - Q_t) = \ln Q_e - k_1 t$	k_1 - Pseudo-first-order rate constant (h^{-1})
Pseudo-second-order	$\frac{t}{Q_t} = \frac{1}{k_2 Q_e^{\,2}} + \frac{t}{Q_e}$	k_2 - Pseudo-second-order rate constant ($mg \cdot g^{-1} \cdot h^{-1}$)
Elovich	$Q_t = \left(\frac{1}{b}\right) \ln(ab) + \left(\frac{1}{b}\right) \ln t$	a - Initial adsorption rate ($mg \cdot g^{-1} \cdot h^{-2}$) b - Elovich constant ($mg \cdot g^{-1}$)
Weber–Morris	$Q_t = k_3 t^{\frac{1}{2}} + C$	k_3 - Weber–Morris rate constant ($mg \cdot g^{-1} \cdot h^{-1/2}$)

898

Table S3 Adsorption isotherm models

Model	Model equation	Model parameters
Langmuir	$C_e/Q_e = \frac{C_e}{Q_m} + \frac{1}{K_L Q_m}$	Q_m - Maximum adsorption capacity (mg·g^{-1}) K_L - Langmuir constant representing the energy of adsorption (L·mg^{-1})
Freundlich	$lnQ_e = \ln K_F + \frac{1}{n} \ln C_e$	K_F - Freundlich constant indicating the adsorption capacity ((mg·g^{-1}) (L·mg^{-1})$^{1/n}$) n - Freundlich exponent related to the energy distribution of adsorption sites (dimensionless)
Temkin	$Q_e = \frac{RT}{B} ln\, A + \frac{RT}{B} ln\, C_e$	A -Temkin constants (L·g^{-1}) B -Temkin constants (J·mol^{-1}) R - Gas constant (8.314 J·(mol·K)$^{-1}$) T - Absolute temperature (K)
Dubinin–Radushkevich	$\ln Q_e = -\beta\varepsilon^2 + \ln Q_s$ $\varepsilon = RTln(1 + \frac{1}{C_e})$ $E = \frac{1}{\sqrt{2\beta}}$	β - Constant related to the energy of adsorption (mol^2·kJ^{-2}) ε - Polanyi potential Q_s - Theoretical saturation capacity (mol·g^{-1}) E - Activation energy (kJ·mol^{-1})

899 **Table S4** Parameters of kinetic model fitting to the As(III) and As(V) adsorption results

Kinetics models			As(III)		As(V)	
			M_0	M_m	M_0	M_m
Experimental results		$Q_{e,exp}$ (mg·g^{-1})	0.31	2.11	0.42	1.03
Pseudo-first-order		$Q_{e,cal}$ (mg·g^{-1})	0.28	1.64	0.36	0.91
		k_1 (h^{-1})	0.05	0.22	0.08	0.34
		R^2	0.9259	0.8084	0.8313	0.6025
Pseudo-second-order		$Q_{e,cal}$ (mg·g^{-1})	0.33	2.06	0.42	1.07
		k_2 (g·mg^{-1}·h^{-1})	0.17	0.10	0.30	0.32
		R^2	0.7845	0.9728	0.9352	0.9923
Elovich		a (mg·g^{-1}·h^{-1})	0.07	1.89	0.18	2.58
		b (g·mg^{-1})	22.08	3.19	14.73	6.72
		R^2	0.9464	0.9222	0.9363	0.8237
Weber–Morris		k_3 (mg·g^{-1}·h$^{-1/2}$)	0.04	0.21	0.05	0.10
		C (mg·g^{-1})	-0.02	0.44	0.03	0.37
		R^2	0.9699	0.8649	0.9562	0.7435
	I	$k_{3(I)}$ (mg·g^{-1}·h$^{-1/2}$)	0.05	0.43	0.08	0.28
		$C_{(I)}$ (mg·g^{-1})	-0.04	0.09	-0.01	0.13
		R_1^2	0.9428	0.7729	0.9301	0.5291
	II	$k_{3(II)}$ (mg·g^{-1}·h$^{-1/2}$)	0.03	0.14	0.04	0.07
		$C_{(II)}$ (mg·g^{-1})	0.01	0.80	0.06	0.53

R_2^2	0.9614	0.9160	0.9799	0.6936

900

Table S5 Parameters of model fitting to the As(III) and As(V) adsorption isotherms

Isotherm models		As(III)		As(V)	
		M_0	M_m	M_0	M_m
Langmuir	Q_m (mg·g^{-1})	0.47	6.95	1.14	3.16
	K_L (L·mg^{-1})	0.02	0.03	0.01	0.04
	R^2	0.3548	0.9248	0.6872	0.8313
Freundlich	K_F ((mg·g^{-1}) (L·mg^{-1})$^{1/n}$)	0.02	0.32	0.02	0.21
	n	1.63	1.48	1.23	1.72
	R^2	0.6490	0.9908	0.9196	0.9624
Temkin	A (L·g^{-1})	0.30	0.62	0.24	0.56
	B	2.64×10^{4}	0.21×10^{4}	1.34×10^{4}	0.41×10^{4}
	R^2	0.4440	0.9200	0.8942	0.8178
Dubinin–Radushkevich	Q_s (mol·g^{-1})	0.20	2.61	0.40	1.46
	β (mol^2·kJ^2)	6.25×10^{-6}	1.12×10^{-6}	8.19×10^{-6}	1.58×10^{-6}
	E (kJ·mo1^{-1})	282.80	669.35	247.03	561.83
	R^2	0.4780	0.6504	0.8356	0.6520

904 **Table S6** Comparison of the As(III) and As(V) removal capacities for the previously reported ball-milled Fe-containing materials and the material

905 investigated in the present study

Materials	Adsorbed pollutant	Initial concentration ($mg \cdot L^{-1}$)	Maximum capacity ($mg \cdot g^{-1}$)	pH	Equilibration time (h)	Preparation method	References
Hematite-coated Fe_3O_4 particles	As(III)	0.01–0.1	1		9	Ball milling under Ar atmosphere and addition of heptane as a lubricant	Simeonidis et al. (2011)
Fe_2O_3-MnO_2		0.2–2	2.52		10	Mechanical–chemical treatment	Andjelkovic et al. (2014)
Fe_2O_3-TiO_2		5–50	13.86		1	Ball milling; sintering at 700 °C for 1 h	Su et al. (2017)
Limonite		1–100	9.14		12	Mechanical activation with an added dispersion medium	Yan et al. (2019)
Zerovalent iron		1–20	9.12		6	Mechanical activation treatment	Zhang et al. (2021)

Magnetite		5–100	6.94		20	Ball milling	Present study
Hematite-coated Fe_3O_4 particles	As(V)	0.01–0.1	2.1		9	Ball milling under Ar atmosphere and addition of heptane as a lubricant	Simeonidis et al. (2011)
Fe_2O_3-MnO_2		0.2–2	3.08		10	Mechanical–chemical treatment	Andjelkovic et al. (2014)
Nanomagnetite-Zeolite		1–300	5.10		1	Synthetic nanomagnetite in an alkali media; ball milling under N_2 atmosphere	Pizarro et al. (2015)
Fe_2O_3-TiO_2		5–50	15.73		1	Ball milling; sintering at 700 °C for 1 h	Su et al. (2017)
Magnetite enriched particles		1–50	13.88		2	Alkaline cleaning, drying, and grinding in the ball-milling system	Shahid et al. (2019)
Limonite		1–100	8.26		12	Mechanical treatment with an added dispersion medium	Yan et al. (2019)
Magnetite		5–100	3.16		20	Ball milling	Present study

906

907

References

Andjelkovic, I., Nesic, J., Stankovic, D., Manojlovic, D., Pavlovic, M.B., Jovalekic, C., Roglic, G., 2014. Investigation of sorbents synthesised by mechanical–chemical reaction for sorption of As(III) and As(V) from aqueous medium, Clean Technol. Environ. Policy 16, 395–403. https://doi.org/10.1007/s10098-013-0635-1.

Pizarro, C., Rubio, M.A., Escudey, M., Albornoz, M.F., Muñoz, D., Denardin, J., Fabris, J.D., 2015. Nanomagnetite–zeolite composites in the removal of arsenate from aqueous systems. J. Braz. Chem. Soc. 26, 1887-1896. https://doi.org/10.5935/0103-5053.20150166.

Shahid, M.K., Phearom, S., Choi, Y., 2019. Adsorption of arsenic (V) on magnetite-enriched particles separated from the mill scale. Environ. Earth Sci. 78, 65. https://doi.org/10.1007/s12665-019-8066-x.

Simeonidis, K., Gkinis, T., Tresintsi, S., Martinez-Boubeta, C., Vourlias, G., Tsiaoussis, I., Stavropoulos, G., Mitrakas, M., Angelakeris, M., 2011. Magnetic separation of hematite-coated Fe3O4 particles used as arsenic adsorbents, Chem. Eng. J. 168, 1008–1015. https://doi.org/10.1016/j.cej.2011.01.074.

Su, H., Lv, X., Zhang, Z., Yu, J., Wang, T., 2017. Arsenic removal from water by photocatalytic functional Fe2O3–TiO2 porous ceramic, J. Porous Mat. 24, 1227–1235. https://doi.org/10.1007/s10934-017-0362-9.

Yan, X., Shao, J., Wen, Q. Shen, J., 2020. Stabilization of soil arsenic by natural limonite after mechanical activation and the associated mechanisms. Sci. Total Environ. 708, 135118. https://doi.org/10.1016/j.scitotenv.2019.135118.

Zhang, T., Zhao, Y., Kang, S., Bai, H., Gu, W., Fang, D., Komarneni, S., Zhang, Q., 2021. Mechanical activation of zerovalent iron (ZVI) in the presence of CaCO3: Improved reactivity of ZVI for enhancing As(III) removal from water. J. Clean Prod. 286, 124926. https://doi.org/10.1016/j.jclepro.2020.124926.

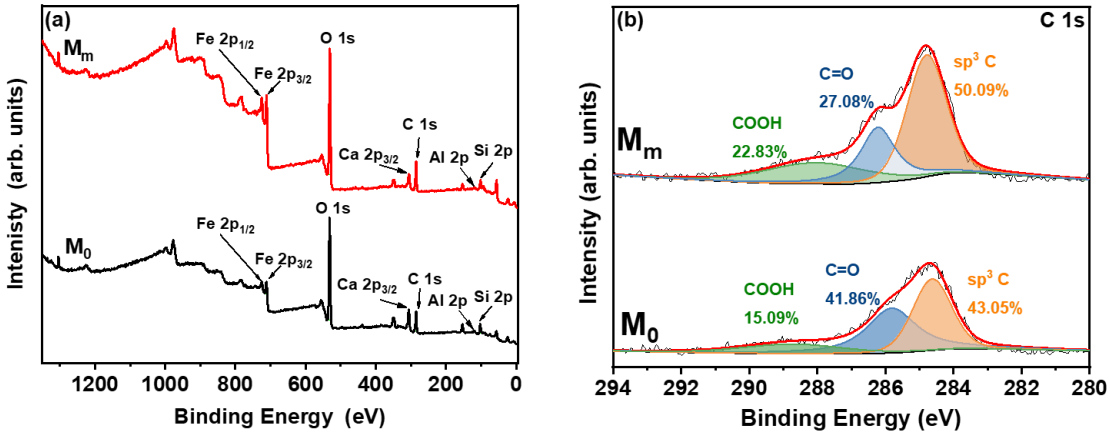

933

934 **Fig. S1** Full (a), and C 1s (b) spectra signals recorded via XPS. M_0 and M_m denote natural

935 magnetite and ball-milled magnetite, respectively.

936

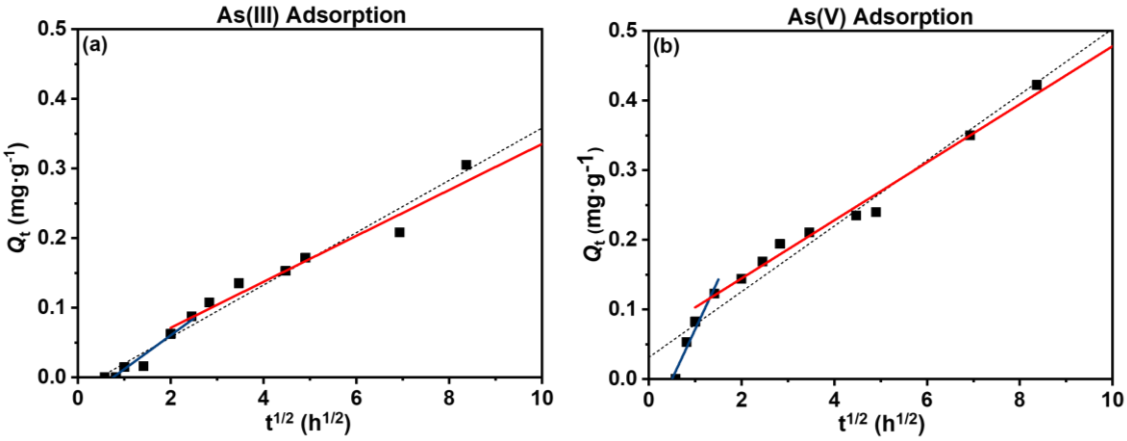

937

938 **Fig. S2** Weber–Morris model plots of As(III) and As(V) on natural magnetite (M_0).

939

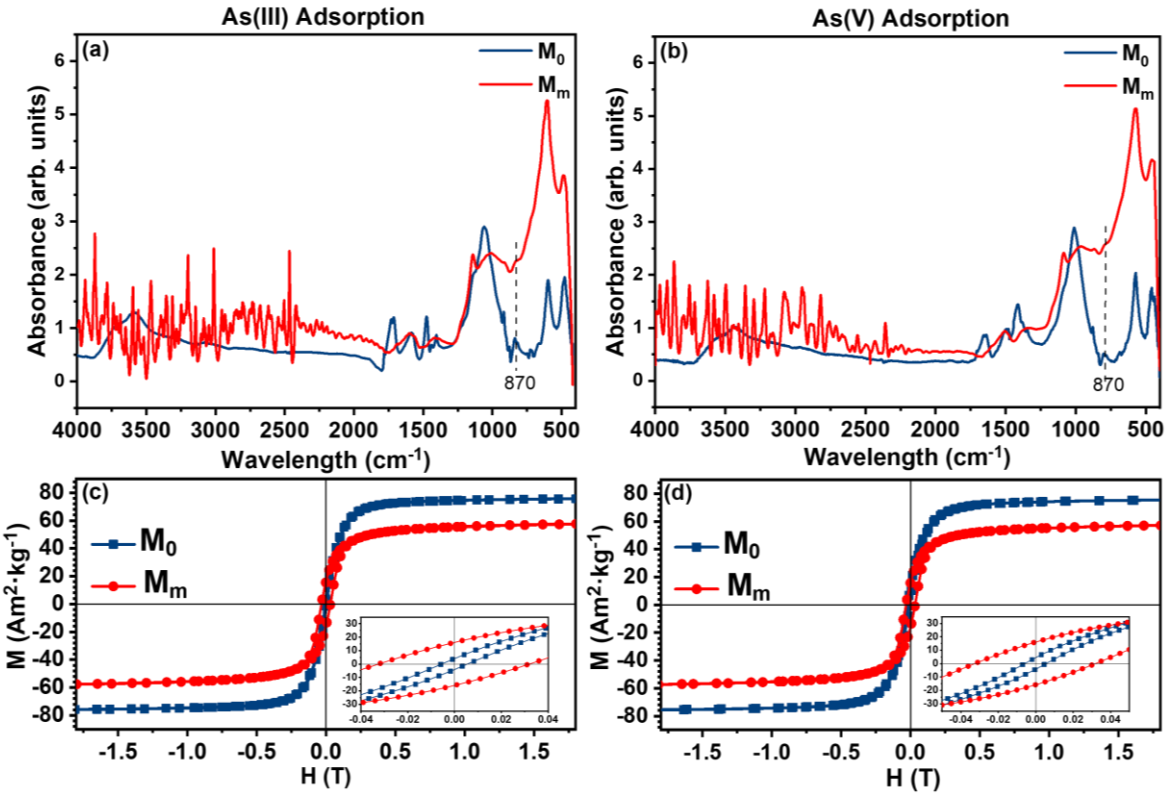

Fig. S3 Variations in the surface chemistry of adsorbents (a, b: FTIR spectra, c, d: magnetic properties recorded via VSM) before and after adsorption of As(III) and As(V). M_0 and M_m denote natural magnetite and ball-milled magnetite, respectively.